



UPPSALA
UNIVERSITET

*Digital Comprehensive Summaries of Uppsala Dissertations
from the Faculty of Science and Technology 2194*

Crystallographic studies of non-equilibrium structural changes in cathode materials

OLOF GUSTAFSSON



ACTA
UNIVERSITATIS
UPSALIENSIS
UPPSALA
2022

ISSN 1651-6214
ISBN 978-91-513-1602-4
URN urn:nbn:se:uu:diva-485227

Dissertation presented at Uppsala University to be publicly examined in Polhemssalen, Ångströmlaboratoriet, Lägerhyddsvägen 1, Uppsala, Friday, 11 November 2022 at 09:00 for the degree of Doctor of Philosophy. The examination will be conducted in English. Faculty examiner: Professor Marnix Wagemaker (Delft University of Technology, The Netherlands).

Abstract

Gustafsson, O. 2022. Crystallographic studies of non-equilibrium structural changes in cathode materials. *Digital Comprehensive Summaries of Uppsala Dissertations from the Faculty of Science and Technology* 2194. 75 pp. Uppsala: Acta Universitatis Upsaliensis. ISBN 978-91-513-1602-4.

Battery cathode materials are a key focus for improvement of Li-ion battery chemistries due their limits in terms of capacity and cost. During insertion and extraction of Li, many cathode materials exhibit structural changes, ranging from e.g. phase transitions to amorphization. Such structural rearrangements can be unfavourable for electrochemical performance due to the incompatibility between any intermediate phases formed. The crystalline structure can be readily studied using diffraction techniques such as X-ray and neutron diffraction, making them a versatile tool for identifying and understanding these structural changes. The work in this thesis focuses on utilizing diffraction to study equilibrium and non-equilibrium changes in the crystalline structure of the two cathode materials $\text{LiNi}_{0.5}\text{Mn}_{1.5}\text{O}_4$ and $\text{Li}_2\text{VO}_2\text{F}$. Both of these materials display interesting structural behaviour upon electrochemical cycling, some of it which can be linked to how the cations arrange in the structure. As such, the work presented here aims to elucidate further on the cationic structural features of these materials and how these may impact their use in batteries.

For both $\text{LiNi}_{0.5}\text{Mn}_{1.5}\text{O}_4$ and $\text{Li}_2\text{VO}_2\text{F}$, the (re)arrangement of cations in the structure was found to play a crucial role for both equilibrium and non-equilibrium structural transitions occurring. In particular, the formation of phases that could be regarded as disadvantageous from a battery application perspective could be attributed to cationic diffusion. Due to the many structural similarities of transition metal oxide-based cathode materials, structural reorganization following similar mechanisms involving cationic rearrangement could be expected also in other materials similar to those studied here. As such, strategies for mitigating any unwanted redistribution of cations in the structure should be considered for improving the performance of this class of cathode materials.

Keywords: Diffraction, Crystallography, Li-ion battery cathode materials, Spinel

Olof Gustafsson, Department of Chemistry - Ångström, Structural Chemistry, Box 538, Uppsala University, SE-751 21 Uppsala, Sweden.

© Olof Gustafsson 2022

ISSN 1651-6214

ISBN 978-91-513-1602-4

URN urn:nbn:se:uu:diva-485227 (<http://urn.kb.se/resolve?urn=urn:nbn:se:uu:diva-485227>)

Till mamma och pappa

List of Papers

This thesis is based on the following papers, which are referred to in the text by their Roman numerals.

- I. **Gustafsson, O.**, Kullgren, J., Brant, W. Low Temperature Cation Ordering in High Voltage Spinel Cathode Material. *Submitted*.
- II. **Gustafsson, O.**, Schökel, A., Brant, W. (2021) Design and Operation of an Operando Synchrotron Diffraction Cell Enabling Fast Cycling of Battery Materials. *Batteries & Supercaps*, 4, 1599–1604.
- III. **Gustafsson, O.**, Schökel, A., Brant, W. Mind the miscibility gap: Cation mixing and current density driven non-equilibrium phase transformations in spinel cathode materials. *Submitted*.
- IV. **Gustafsson, O.**, Baur, C., Valvo, M., Fichtner, M., Brant, W. Electrochemically driven non-equilibrium phase transitions in disordered rock-salt cathode material. *In manuscript*.

Reprints were made with permission from the respective publishers.

Disclaimer: Parts of this Thesis is based on the author's licentiate thesis entitled "Non-equilibrium structural changes in rock-salt derived cathode materials" (Uppsala University, 2021).

Comments on the authors contribution to the papers:

- I. Prepared all material for the *in situ* measurements. Planned and analysed the neutron diffraction experiments. Performed all in-house measurements, except thermal analysis and mass spectroscopy. Wrote the manuscript with input from the co-authors.
- II. Designed the *operando* cell setup. Prepared material for and performed assembly of battery cells for *operando* measurements. Planned and analysed the *operando* experiments. Advised and assisted in carrying out the *operando* measurements remotely. Wrote the manuscript with input from the co-authors.
- III. Prepared material for and performed assembly of battery cells for *operando* measurements. Planned and analysed the *operando* experiments. Advised and assisted in carrying out the *operando* measurements remotely. Wrote the manuscript with input from the co-authors.
- IV. Carried out battery cell assembly and electrochemical characterisation. Planned and analysed the neutron diffraction experiments. Carried out neutron diffraction measurements with the assistance from the beamline scientist. Carried out some and analysed all X-ray diffraction experiments. Wrote the manuscript with input from the co-authors.

Related work

In addition, the author has also contributed to the following work not included in this thesis:

- I. Mozhzhukina, N., Kullgren, J., Baur, C., **Gustafsson, O.**, Brant, W., Fichtner, M., Brandell, D. (2020) Short-range ordering in the Li-rich disordered rock salt cathode material $\text{Li}_2\text{VO}_2\text{F}$ revealed by Raman spectroscopy. *J Raman Spectrosc.*, 51, 2095-2101.

Contents

1.	Introduction.....	13
1.1.	Li-ion batteries	13
1.2.	Battery cathode materials	16
1.2.1.	Crystallography	17
1.2.2.	Linking structure and electrochemical performance.....	19
1.2.3.	Structural changes originating from electrochemical cycling	20
2.	Thesis scope.....	23
3.	Methodology.....	25
3.1.	Material synthesis	25
3.1.1.	Preparation of disordered and ordered $\text{LiNi}_{0.5}\text{Mn}_{1.5}\text{O}_4$	25
3.1.2.	Synthesis of $\text{Li}_2\text{VO}_2\text{F}$	25
3.1.3.	Chemical delithiation	25
3.2.	Battery cell assembly and electrochemical characterization	26
3.2.1.	Electrode preparation and cell assembly	26
3.2.2.	Galvanostatic cycling.....	27
3.3.	Material characterization	27
3.3.1.	Powder diffraction.....	27
3.3.2.	Structure analysis based on diffraction data.....	29
3.3.3.	Diffraction peak shape modelling.....	30
3.3.4.	Inductively coupled plasma optical emission spectroscopy	32
4.	Results and discussion.....	33
4.1.	Cationic ordering behaviour in $\text{Li}_x\text{Ni}_{0.5}\text{Mn}_{1.5}\text{O}_4$	33
4.1.1.	Structural characterization of $\text{Li}_x\text{Ni}_{0.5}\text{Mn}_{1.5}\text{O}_4$	33
4.1.2.	Structural changes in $\text{Li}_x\text{Ni}_{0.5}\text{Mn}_{1.5}\text{O}_4$ during heating.....	35
4.1.3.	Linking structural changes to cation rearrangement in $\text{Li}_x\text{Ni}_{0.5}\text{Mn}_{1.5}\text{O}_4$	39
4.2.	Phase transition mechanisms in $\text{LiNi}_{0.5}\text{Mn}_{1.5}\text{O}_4$ during electrochemical cycling	42
4.2.1.	The <i>operando</i> pouch cell holder.....	42
4.2.2.	Characterization of the degree of Ni and Mn ordering	46
4.2.3.	<i>Operando</i> X-ray diffraction	47

4.2.4.	Identifying phase transition mechanisms from diffraction	51
4.2.5.	Quantifying changes in the miscibility gap and assessing phase transition mechanisms	52
4.3.	Structural changes in $\text{Li}_2\text{VO}_2\text{F}$ during prolonged electrochemical cycling	56
4.3.1.	Structural characterization of $\text{Li}_x\text{VO}_2\text{F}$	56
4.3.2.	Prolonged cycling of $\text{Li}_2\text{VO}_2\text{F}$	58
4.3.3.	Anionic redox behaviour and cationic reorganization	59
5.	Conclusions	63
	Sammanfattning på Svenska	65
	Acknowledgements	68
	References	70

Abbreviations

CB	Carbon black
DEC	Diethyl carbonate
DFT	Density functional theory
DMC	Dimethyl carbonate
DRS	Disordered rock-salt
EC	Ethylene carbonate
FWHM	Full width at half maximum
ICP-OES	Inductively coupled plasma optical emission spectroscopy
LFP	LiFePO_4
LNO	$\text{Li}_{0.4}\text{Ni}_{1.6}\text{O}_2$
LNMO	$\text{LiNi}_{0.5}\text{Mn}_{1.5}\text{O}_4$
LMO	$\text{Li}_{0.05}\text{Mn}_{0.95}\text{O}_2$
NCA	$\text{LiNi}_{0.8}\text{Co}_{0.15}\text{Al}_{0.05}$
ND	Neutron diffraction
NMC	$\text{LiNi}_{1/3}\text{Mn}_{1/3}\text{Co}_{1/3}\text{O}_2$
NMP	N-methyl-2-pyrrolidone
OCV	Open-circuit voltage
PDF	Probability density function
PVDF	Polyvinylidene difluoride
RIXS	Resonant inelastic X-ray scattering
SF	Scale factor
SOC	State of charge
TEM	Transmission electron microscopy
TM	Transition metal
XRD	X-ray diffraction

1. Introduction

1.1. Li-ion batteries

In light of the recently released first part of the sixth report on climate change by the Intergovernmental Panel on Climate Change (IPCC), concerns are once again being intensified about climate change and its potentially severe effect on the environment and society.¹ It is evident that a shift away from fossil fuels towards more sustainable and environmentally friendly sources of energy is necessary in order to limit the inevitable impact from greenhouse gas emissions. A key technology for realizing this shift is the implementation of batteries for energy storage applications both on and off the grid. As an example, the European Commission recently proposed that, as a part of the European Union reaching its goal of a 55% cut in emissions by 2030 (compared to 1990 levels), CO₂ emissions from all new cars should be reduced by 55% by 2030 and effectively reach zero by the year 2035.² The need for electric vehicles to facilitate this transition is evident and highlights just one example of where rechargeable batteries will continue to be an important technology for reducing global emissions.

The Li-ion battery has so far played a big role in the widespread use of rechargeable batteries, in applications ranging from portable electronics to electric vehicles. Even though other technologies, such as Na-ion batteries, are currently on the rise, the impact and relevance of the Li-ion battery still remain strong today, and will continue to do so, roughly 30 years after its commercialization. The inception of the Li-ion battery is credited to the collective work of Stanley Whittingham, John Goodenough, and Akira Yoshino, who shared the Nobel Prize in Chemistry in 2019 for their individual contributions toward the development of the Li-ion technology. The working principle of a Li-ion battery is best described by looking at its main components; the positive electrode (commonly referred to as the cathode), the negative electrode (commonly referred to as the anode), electrolyte and separator, as shown in Figure 1. The cathode and anode are often referred to as the electrodes and these act as host materials where Li-ions can move in and out of the structure, also known as insertion and extraction, respectively. As the redox reactions that enable the generation of a current from the battery take place, Li-ions are either inserted to or extracted from the electrodes, while electrons simultaneously move through an outer circuit connecting the electrodes. By integrating a device/load in the outer circuit, the electrons can then

perform electrical work. The electrolyte acts as a conducting medium for the Li-ions to travel between the two electrodes and simultaneously preventing electronic conduction, while the separator acts as a physical barrier between the electrodes to prevent short-circuiting of the battery. As all the components in the battery contribute to its functional operation, there are many complex processes occurring within and at the surfaces of each material component during battery use. Understanding the different processes is a challenging task and involves several facets of chemistry such as electrochemistry, characterization of surface reactions and structural characterization of the bulk materials. As such, research focused on battery chemistries is a collective effort where a plethora of techniques are needed to study the different components and processes to piece together the puzzle of battery operation. Further complications arise due to the various ways of combining different materials and components to create a functioning battery chemistry, resulting in a range of interesting materials to study for creating new battery technologies.

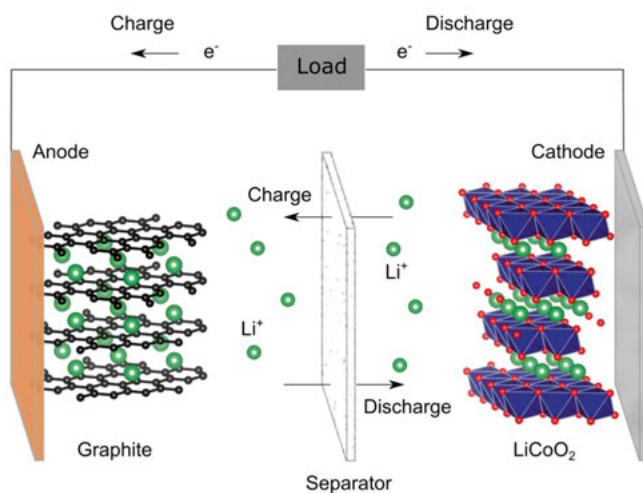


Figure 1. Illustration of the working principle of a rechargeable Li-ion battery, utilizing graphite as anode and LiCoO₂ as cathode. Their respective current collectors are typically composed of Cu and Al.

As a starting point for looking closer at the electrode materials, let us return to the pioneering work that resulted in the commercialization of Li-ion batteries. The first Li-ion battery prototype, developed by Whittingham in 1976, was based on a lithium metal anode and a TiS₂ (or LiTiS₂ when lithiated) cathode able to accommodate Li-ions through electrochemical insertion.³ The concept was then further developed by Goodenough a few years later by replacing LiTiS₂ with LiCoO₂ as the cathode material.⁴ Both of these battery prototypes utilized Li metal as the anode, forming a cell system also known as a Li half-

cell. Due to a series of safety issues related to using Li metal and its plating/stripping reactions, researchers looked into different types of anode materials which could also host Li-ions through an alternative insertion mechanism, which resulted in the development of an anode based on petroleum coke by Yoshino.⁵ This anode material containing graphitic features could successfully accommodate Li-ions. When paired with a LiCoO₂ cathode it ultimately constituted a safer working full-cell battery prototype. The key to the success of the Li-ion battery technology lies in the highly reversible electrochemical insertion and extraction of Li-ions within the electrode materials during charge and discharge. Focusing on the cathode side, the process is enabled by the structure of the materials, wherein the Li-ions can be accommodated, as shown in Figure 2, in addition to the redox reactions enabling the formation of an electric current. The crystalline cathode materials have a structure where certain crystallographic sites can be occupied by the Li-ions as they are inserted in the structure upon discharge. This insertion of Li-ions in the structure can be understood from the charge compensation mechanism taking place in order for the cathode material to remain charge neutral. Using discharge in LiCoO₂ as an example, Co⁴⁺ gets reduced to Co³⁺, and to maintain charge neutrality in the compound, Li-ions are inserted in the structure. In the case of both LiTiS₂ and LiCoO₂, the structures are layered, alternating between layers of transition metals (TM), here either Ti or Co, and an anionic species X, here S or O, and layers of Li. Other currently employed cathode materials such as LiMn₂O₄ and LiFePO₄ adopt different crystal structures and sites for Li occupation. Depending on the type of structure and how Li is hosted therein, different pathways of Li insertion and extraction exist, thus linking the electrochemical and crystallographic properties of different cathode materials.

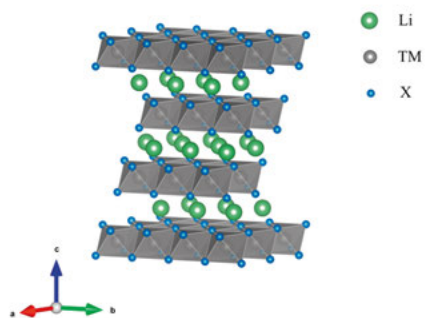


Figure 2. General crystal structure of a layered LiTMX₂ material.

1.2. Battery cathode materials

A large portion of the research interest in battery development is directed toward cathode materials, mainly due to two reasons; the cathode can contribute to roughly half of the total cost of the entire battery cell (in terms of cost per kWh)⁶ and often represents the limiting factor with respect to the specific capacity (mAh g⁻¹). Adding to this, concerns about sustainability, ethics, and natural abundance of some of the raw materials utilized, such as Co, lead researchers to search for different types of cathode materials. Many of the popular cathode materials for Li-ion batteries, both commercially available and still under research, are based on 3d transition metals (TM), such as the previously mentioned LiCoO₂, LiFePO₄ and LiMn₂O₄. Historically, the most popular transition metal oxide materials are based on the layered LiCoO₂ and LiMn₂O₄ structure, also known as spinel (Figure 3). Substitution with other 3d transition metals such as Ni, Mn, and Al, have led to the main commercialized compounds, such as layered LiNi_{1/3}Mn_{1/3}Co_{1/3}O₂ (NMC) and LiNi_{0.8}Co_{0.15}Al_{0.05} (NCA) and spinel LiNi_{0.5}Mn_{1.5}O₄ (LNMO), providing a range of different cathode materials with distinctive electrochemical features. More recently, different types of Li-rich cathode materials have also gained interest, such as layered Li-rich transition metal oxides, e.g. Li₂MnO₃, and Li-rich disordered rock-salt (DRS) materials (Figure 3), e.g. Li₂VO₂F or Li₂Mn_{2/3}Nb_{1/3}O₂F, due to their high theoretical capacity.

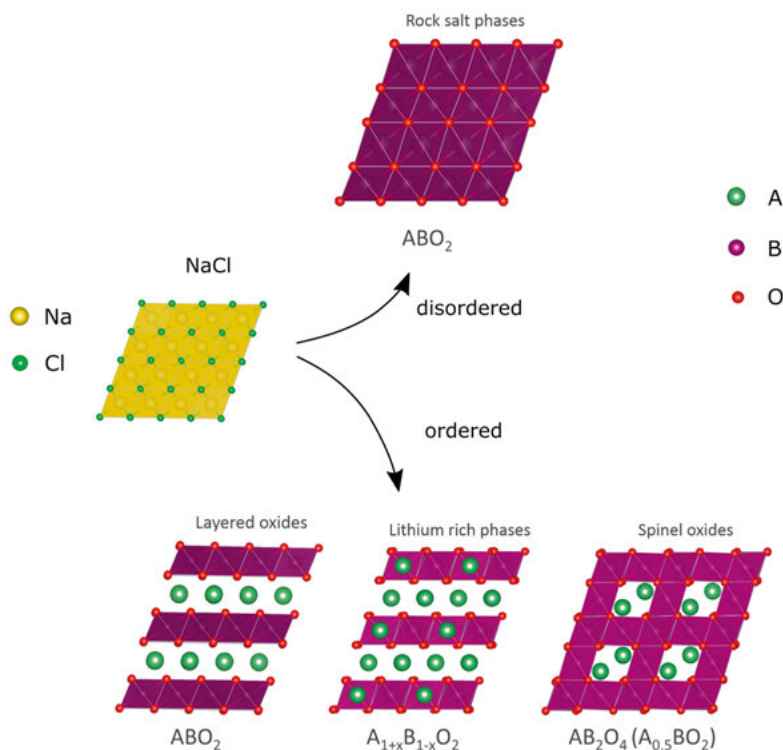


Figure 3. Illustration of the structure relation between different rock-salt derived materials. In battery cathode materials, A is usually Li-ions and B is usually one or more transition metals. As shown in the illustration, the structure types can be categorized into disordered (rock-salt phases) and ordered (layered, lithium rich layered and spinel) structure types.

1.2.1. Crystallography

Although at a first glance the structures of different transition metal oxide-based materials may seem quite different to one another, they can be derived from a common ‘parent’ structure analogous to the simple rock-salt structure of NaCl, as highlighted in Figure 3. As shown in Figure 4a, the structure of NaCl can be viewed as a cubic close packing of Cl⁻ anions, with Na⁺ ions in the octahedral holes and subsequently octahedral coordination between the anions and cations. Due to the symmetry of the unit cell describing the crystal structure, the position of the anions and the cations can be described by two distinct crystallographic sites, also known as Wyckoff positions⁷. In the cubic NaCl rock-salt structure, the cations occupy the $4a$ position (0, 0, 0) and the anions occupy the $4b$ position (0.5, 0.5, 0.5). The symmetry of this structure can be described in the crystallographic space group $Fm\bar{3}m$. Along the [111] direction, the anions and cations appear to organize in alternating layers, as shown in Figure 4b.

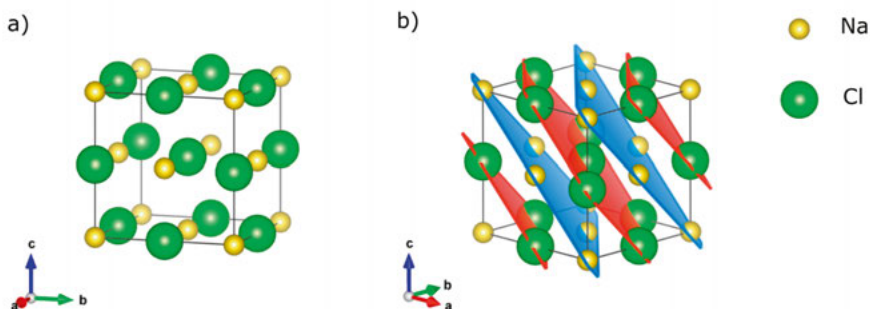


Figure 4. a) Crystal structure of NaCl and b) alternating cationic (blue) and anionic (red) layers normal to the $[111]$ direction highlighted.

The DRS, layered and spinel structures can be derived from the NaCl structure by first exchanging Cl⁻ with O²⁻ anions at the $4b$ positions. Depending on how the cations are distributed over the octahedral and tetrahedral sites in the anionic framework, different structures can then be obtained. The Li-rich DRS structure of Li₂VO₂F is achieved if Na⁺ is replaced by Li⁺ and V³⁺, which are distributed randomly over the $4a$ position. Additionally, a third of the O²⁻ anions are randomly replaced by F⁻, see Figure 5a. The layered structure, e.g. LiCoO₂ (Figure 2), is obtained by replacing Na⁺ with Li⁺ and Co³⁺, which then occupy alternating cation layers normal to the $[111]$ direction in the parent NaCl rock-salt unit cell. Finally, the spinel structure (space group $Fd\bar{3}m$) is a little more complex, where half of the octahedrally coordinated sites are occupied by TM cations in the $16c$ position, with Li occupying one eighth of the tetrahedrally coordinated sites in the $8b$ position, as exemplified by the structure of LiNi_{0.5}Mn_{1.5}O₄ illustrated in Figure 5b.

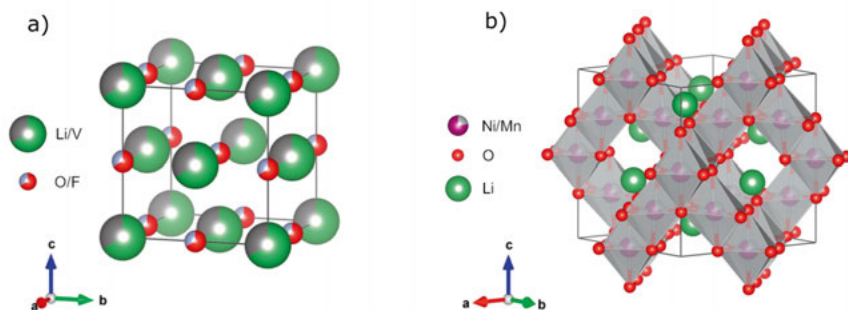


Figure 5. a) DRS structure of Li₂VO₂F, and b) spinel structure of LiNi_{0.5}Mn_{1.5}O₄.

To summarize, all three different structure types brought up here can be viewed as a network of edge-sharing octahedra with face-shared tetrahedra in

between, existing in a cubic close packed anionic framework common to all three structures. Depending on how the cations order within this framework, the type of structure is determined.

1.2.2. Linking structure and electrochemical performance

The relationship between structure and electrochemical performance is multifaceted, due to how electrochemical performance is defined and how the structure then relates to that definition. In this thesis, the electrochemical performance is considered from the viewpoint of capacity loss (or retention) over prolonged cycling and rate capability. The relationship between structure and capacity loss will be discussed in the next section, while rate capability will be explained further here.

Rate capability is the ability of a material to deliver a stable capacity when cycled at an increased current. That is, a material with good rate capability should display little voltage polarization as the current is increased. Good rate capability is an important factor when considering specifically the high-rate performance of battery materials. In applications that require fast charging, e.g. electric vehicles, a good rate capability is necessary to efficiently store the electric energy in the battery. The rate-limiting step in a Li-ion battery is often the Li-ion diffusion in the solid state, i.e. in the electrode materials, which is a relatively slow process compared to the diffusion in the electrolyte.⁸ As such, the rate capability can be improved either by shortening the diffusion length (e.g. reducing the particle size), or by increasing the diffusivity. The connection between structure and diffusivity, and therefore also the rate capability, can be understood from looking at how Li-ion diffusion occurs in these materials. Generally, Li-ions diffuse by moving between different vacant octahedral and tetrahedral sites within the structure. In the DRS and layered structures, Li-ions diffuse from an octahedral site to an adjacent vacant edge-sharing octahedral site via an empty tetrahedral site, see Figure 6.⁹⁻¹²

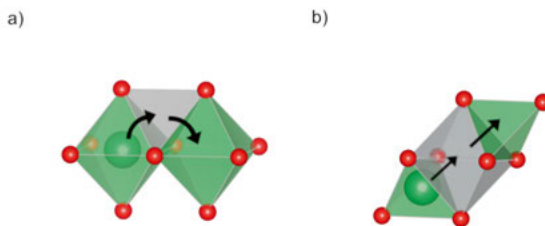


Figure 6. Illustration of Li-ion diffusion between a) two octahedral sites through a tetrahedral site and b) two tetrahedral sites through an octahedral site.

This diffusion to a tetrahedral site is associated with an activation energy, which is determined by electrostatic interactions between the lithium ion and the cations in the octahedra adjacent to the tetrahedral site.^{9-10,12} As these moves, or ‘hops’, are facilitated by thermal energy fluctuations, the hopping rate will be determined by the activation energy of the move.¹² Ultimately, the activation energy can thus be linked to Li-ion diffusion and will further affect the rate at which Li-ions can be inserted and extracted during discharge and charge, respectively. In the spinel structure, Li-ions diffuse by moving between two tetrahedral sites, through a vacant octahedral site.¹³ Similarly, Li-ion diffusion in the spinel structure will be determined by the activation energy of the migration to the empty octahedral site. However, Li-ions are not the only species in the structure that can diffuse, as other cationic species, i.e. transition metals, have also been found to rearrange during electrochemical cycling. For example, in $\text{LiNi}_{0.5}\text{Mn}_{1.5}\text{O}_4$, Ni and Mn were observed to rearrange upon repeated electrochemical Li extraction and insertion.¹⁴ Not only does such reorganization block the Li-ion diffusion pathways, e.g. via Ni and Mn diffusion to vacant octahedral sites in $\text{LiNi}_{0.5}\text{Mn}_{1.5}\text{O}_4$ ¹⁵, but can also lead to a structural configuration with different electrochemical properties. In the case of $\text{LiNi}_{0.5}\text{Mn}_{1.5}\text{O}_4$, the configuration of Ni and Mn in the structure will affect the Li-ion diffusivity in the material, which further influences the rate capability of the material.¹⁶⁻¹⁷

1.2.3. Structural changes originating from electrochemical cycling

During electrochemical insertion and extraction of Li-ions, many cathode materials exhibit structural changes, ranging from e.g. phase transitions to amorphization.¹⁸⁻²² Since the electrochemical properties of a battery cathode material, such as Li-ion diffusivity, depend on the structure of the material, knowledge about these structural changes is key to understanding their high-rate performance. Further, moving beyond the local atomic scale, changes in the structure also influence the electrochemical performance of processes occurring at the crystallite/particle scale. For example, active materials that undergo structural rearrangements are generally seen as unfavourable when there is incompatibility between the intermediate phases formed. If there are large volume and structural framework mismatches between two co-existing structures within the active material, this can lead to kinetic barriers and also strain in the material. The kinetic barriers limit the rate at which Li-ions can be extracted or inserted, while also leading to inhomogeneity across the material during operation, decreasing the accessible capacity.²³ Large strain may also result in a decreased capacity due to particle cracking and subsequent loss of electrical contact. In order to improve existing battery materials by eliminating

unwanted structural rearrangements, an understanding of why they occur and how this relates to the original atomic arrangement in the structure is clearly needed.

Two experimental approaches are commonly employed when studying structural changes originating from electrochemical cycling. The first is the *ex situ* (Latin, roughly translates to ‘off site’) approach, where the material under investigation is first electrochemically cycled in a battery, which is then disassembled, and the material is extracted for characterization. *Ex situ* studies can provide useful information on the equilibrium structure of a material following lithium insertion or extraction, however, any intermediate changes or states occurring during operation may not be seen. Further, *ex situ* methods provide a simple experimental route, since there is no need for specialized experimental setups, and a good starting point to identify structural changes. The second approach would be to perform a so-called *operando* measurement, in which the material is studied during operation in a device, i.e. under ‘real’ conditions. When studying battery materials, many structural changes that occur involve metastable intermediate states or non-equilibrium phase transitions, making *operando* techniques an essential tool. The inability to capture intermediate structures of battery materials using an *ex situ* approach makes *operando* measurements desirable for unravelling the full structural mechanism of lithium insertion and extraction. Another interesting aspect when studying the structure of battery materials under *operando* conditions is the ability to capture non-equilibrium intermediate phases that occur during electrochemical cycling at elevated rates. In LiFePO_4 , the material undergoes a two-phase reaction between the two end phases LiFePO_4 and FePO_4 during chemical (de)lithiation and electrochemical cycling at slow rates.²⁴ When cycled at a high rate, however, the material can be forced into a non-equilibrium solid solution-type reaction instead, driven by an increased overpotential.²⁵⁻²⁶ This type of structural behaviour involving non-equilibrium phases highlights the need for suitable *operando* measurements. Design of effective *operando* setups may not be trivial and poses some challenges in achieving setups which can facilitate equivalent, or as close to, ‘real’ conditions as in a normal battery cell. Simultaneously, any setup should provide good enough measurement conditions for accurate tracking of any changes occurring to the active materials and/or other cell components. These design criteria become especially important when performing *operando* measurements at higher currents, which impose further limitations. From an electrochemical perspective, issues arising from internal resistances, such as ohmic polarisation, are amplified at higher currents. Ohmic polarisation can act as a practical limitation toward studies performed at high rates if the cut-off voltages are not adjusted to account for the added resistance. From the perspective of diffraction, high rates require shorter data collection times for adequate time-resolved tracking of any structural changes. This often requires modification of the cell design so as to reduce absorption and scattering from the inactive materials. However,

disrupting the integrity of standard battery cell designs, such as coin cells and pouch cells, often leads to a worsened electrochemical performance.²⁷⁻²⁹ One example of an often employed design is the modification of a standard coin cell, where a hole is drilled in the casing, sealed with Kapton® tape.²¹ This modification is done to reduce the amount of inactive material in the beam and to increase the proportion of the total scattering from the active material and reduce absorption. However, such a modification leads to a loss of stack pressure at the position of the hole, due to the flexibility of the tape sealing, resulting in an increased cell resistance.²⁸ Designs utilizing a similar approach as the Kapton® modified coin cell highlight the main issue for *operando* battery experiments and setups; obtaining comparable electrochemical performance to standard battery cells while simultaneously minimizing contributions to the resulting diffraction patterns from the inactive materials.

Another experimental approach that can be taken when trying to understand the underlying mechanism or driving force for any observed structural transformation are *in situ* ('on site') measurements. The term *in situ* covers a broad spectra of measurement conditions, nevertheless it can be distinguished from *ex situ* in the sense that the measured material is undergoing changes during the measurement. The term *in situ* is also differentiated from *operando* from the point that during *operando* conditions the material is not only undergoing changes, but it is simultaneously performing 'work' based on its intended function, e.g. electrochemical cycling in a battery. A typical example of an *in situ* measurement is to observe changes in a material when it is undergoing heating. Such a measurement can provide insights into the thermodynamic barriers for structural changes to occur, aiding with understanding the pathway taken for structural transitions that occur *operando*. As an example, the difference in structural behaviour for LiFePO_4 at conditions further away from equilibrium, i.e. at increasing overpotentials, could be understood from the observed formation of metastable $\text{Li}_{1-x}\text{FePO}_4$ solid solutions from $\text{LiFePO}_4/\text{FePO}_4$ two-phase mixtures at elevated temperatures.^{26,30}

2. Thesis scope

The work in this thesis revolves around studying changes in the crystalline structure of battery cathode materials under both equilibrium and non-equilibrium conditions. Specifically, how cationic arrangements in the structure of two rock-salt derived materials, $\text{LiNi}_{0.5}\text{Mn}_{1.5}\text{O}_4$ and $\text{Li}_2\text{VO}_2\text{F}$, influences their respective structural behaviour during electrochemical cycling. The main characterization tool used for this purpose was diffraction, both with X-rays and neutrons. The work will also highlight how the different characterisation approaches *ex situ*, *in situ* and *operando* can be applied to study and understand structural behaviour that arises during electrochemical cycling. While providing different advantages and drawbacks, all three approaches can provide useful and unique insights, which this thesis aims to highlight.

In the first part of the thesis, the thermal equilibrium phase transitions in $\text{Li}_x\text{Ni}_{0.46}\text{Mn}_{1.54}\text{O}_4$ ($0 \leq x \leq 1$) were explored as a means of explaining the previously reported transition from transition metal disordered to ordered LNMO during galvanostatic cycling.¹⁴ More specifically, applying *in situ* neutron diffraction to determine the role of cationic rearrangement mechanisms driving the observed phase transitions in LNMO (Paper I).

In the second part, based on the understanding that LNMO can transition from its disordered to ordered form upon electrochemical cycling, the differences in structural behaviour between the two during operation in a battery were explored. Electrochemical processes do not occur at thermodynamical equilibrium, so as to develop an understanding of the mechanism behind the structural behaviour of disordered and ordered LNMO, their respective non-equilibrium phase transitions were studied *operando* (Paper II and III). The combined work presented in the first two parts provide insights on the role of cation arrangement for the formation of equilibrium and non-equilibrium phases in LNMO.

The third part then focuses on what role the (re)arrangement of cations play in the formation of equilibrium and non-equilibrium phases in another rock-salt derived material, sharing structural similarities to LNMO, namely $\text{Li}_2\text{VO}_2\text{F}$ (Paper IV). That is, if similar concepts of cationic rearrangement found in LNMO also can be seen in $\text{Li}_2\text{VO}_2\text{F}$ when operated in a battery. Due to the disordered and nanocrystalline nature of $\text{Li}_2\text{VO}_2\text{F}$, *in situ* and *operando* techniques are quite challenging for observing significant changes in its structure. Therefore, in order to acquire high quality diffraction data, while also

studying the long-term behaviour from electrochemical cycling, an *ex situ* approach was applied.

3. Methodology

3.1. Material synthesis

3.1.1. Preparation of disordered and ordered $\text{LiNi}_{0.5}\text{Mn}_{1.5}\text{O}_4$

Transition metal disordered and ordered LNMO was prepared from commercially available powders via heat treatment. The ordering process in LNMO is typically initiated at temperatures above 700 °C and different degrees of ordering can be obtained by varying the annealing time above this temperature and the rate of cooling. Disordered LNMO is generally obtained by annealing for a shorter time period followed by rapid cooling via quenching of the powder. Nearly fully ordered LNMO can be obtained by increasing the annealing time and then employing a slower cooling down to room temperature. Specific details on this process can be found in Paper I and Paper III.

3.1.2. Synthesis of $\text{Li}_2\text{VO}_2\text{F}$

The disordered rock-salt structure of $\text{Li}_2\text{VO}_2\text{F}$ is metastable and has so far only been synthesized using either high-energy ball-milling or a high temperature, high pressure route.³¹⁻³⁶ In this work, the material was synthesized via ball-milling of the precursors V_2O_3 , Li_2O and LiF under Ar atmosphere. Since the work presented in this thesis is more focused on the characterization aspects, the synthesis will not be extensively discussed here, however, it has been thoroughly described elsewhere.^{33,37} Due to the instability of the DRS $\text{Li}_2\text{VO}_2\text{F}$, all further handling and treatment of the material following its synthesis were carefully performed under Ar atmosphere.

3.1.3. Chemical delithiation

Chemical delithiation is a process in which an oxidizing agent is added to the cathode material, often in the form of a solution. In order for the oxidized compound to remain charge neutral, Li-ion extraction from the structure occurs. Commonly employed oxidizing agents are e.g. Br_2 , I_2 or NO_2BF_4 . Chemical delithiation favours formation of thermodynamically stable phases if done over a long time-domain. In addition, the chemical delithiation route provides a more practical alternative for preparing the large sample quantities (order of

grams) needed for neutron diffraction, as compared to electrochemical delithiation in e.g. a battery cell. As such, chemical delithiation was chosen as a method for obtaining a series of thermodynamically stable members from $\text{Li}_x\text{Ni}_{0.5}\text{Mn}_{1.5}\text{O}_4$ ($0 \leq x \leq 1$) and $\text{Li}_y\text{VO}_2\text{F}$ ($0 \leq y \leq 2$). The $\text{Li}_x\text{Ni}_{0.5}\text{Mn}_{1.5}\text{O}_4$ samples were prepared using NO_2BF_4 , while $\text{Li}_y\text{VO}_2\text{F}$ samples were prepared with I_2 and Br_2 as the oxidizing agents, with acetonitrile as the solution. The powdered samples were left stirring in solution for one week, followed by washing with additional acetonitrile before drying under vacuum.

3.2. Battery cell assembly and electrochemical characterization

3.2.1. Electrode preparation and cell assembly

Composite electrodes of $\text{LiNi}_{0.5}\text{Mn}_{1.5}\text{O}_4$ and $\text{Li}_2\text{VO}_2\text{F}$ were prepared by mixing the active material with a polymer binder (polyvinylidene difluoride, PVDF) dissolved in N-methyl-2-pyrrolidone (NMP) and a conductive carbon additive (carbon black, CB). The composite electrode slurry mixtures were then ball-milled followed by casting on Al foil and drying the film. The resulting 19.8 x 11.1 cm rectangular composite $\text{Li}_2\text{VO}_2\text{F}$ cast electrodes were purposely kept as obtained after drying for cell assembly, while circular 13 mm diameter electrodes were punched out for the composite $\text{LiNi}_{0.5}\text{Mn}_{1.5}\text{O}_4$ cast electrodes. The resulting thickness of the $\text{Li}_2\text{VO}_2\text{F}$ composite electrodes was $\approx 100 \mu\text{m}$, with a mass loading of 1.5 mg cm^{-2} . The $\text{LiNi}_{0.5}\text{Mn}_{1.5}\text{O}_4$ were prepared in two different mass loadings/thicknesses, i.e. $5 \text{ mg cm}^{-2}/25 \mu\text{m}$ and $2 \text{ mg cm}^{-2}/10 \mu\text{m}$.

For both cathode materials, the composite electrodes were assembled in pouch cells, see Figure 7, employing Li metal foil as combined negative and reference electrode. For $\text{Li}_2\text{VO}_2\text{F}$, glass fibre filters were used as separator with 1 M LiPF_6 in ethylene carbonate/dimethyl carbonate (EC/DMC, 1:1 volume ratio) as the electrolyte. Due to the need for larger sample volumes in neutron diffraction, an up-scaled pouch cell was assembled in this case, see Figure 7a. For $\text{LiNi}_{0.5}\text{Mn}_{1.5}\text{O}_4$, a polypropylene/polyethylene-based membrane (Celgard 2325) was used as separator with 1 M LiPF_6 in ethylene carbonate/diethyl carbonate (EC/DEC, 1:1 volume ratio) as the electrolyte.

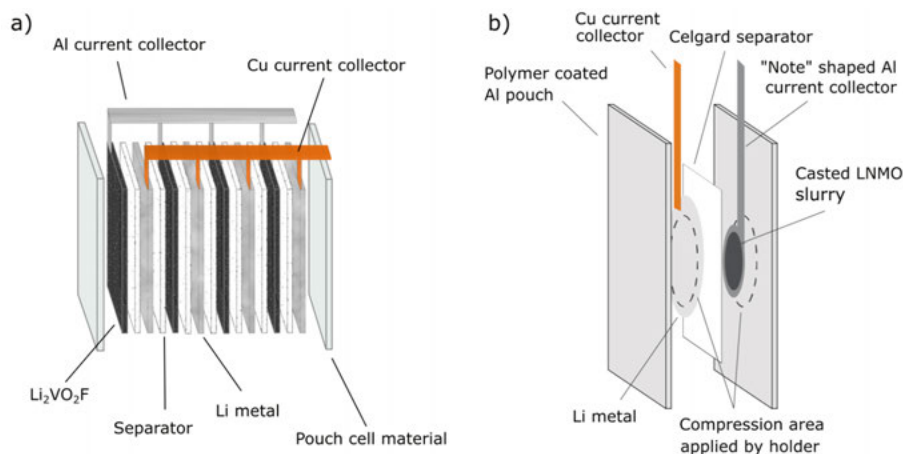


Figure 7. Illustration of the two different types of pouch cells utilized for a) $\text{Li}_2\text{VO}_2\text{F}$ and b) $\text{LiNi}_{0.5}\text{Mn}_{1.5}\text{O}_4$ cycling, respectively. Figure adapted from Paper II and IV.

3.2.2. Galvanostatic cycling

Electrochemical characterization and operation of the assembled battery cells were carried out by galvanostatic cycling. In galvanostatic cycling, a constant current (in absolute terms) is controlled over time during charge and discharge, while the cell voltage is recorded. The controlled current can often be seen referred to as the C-rate. The C-rate is based on the theoretical capacity, $C_{\text{theoretical}}$ (mAh g^{-1}), of the active material being cycled, for which a rate of 1C corresponds to a full charge or discharge completed in 1 hour. More generally, the C-rate can be seen as the reciprocal of the time, expressed in hours, needed for a complete charge or discharge, with a rate of $C/2$ corresponding to charge (or discharge) completion in 2 hours, for example. Consequently, the controlled current at a specific C-rate will be dependent on the mass of the material that is being cycled and its theoretical capacity.

3.3. Material characterization

3.3.1. Powder diffraction

In this section, the principles of powder diffraction will be discussed briefly. For a more in-depth review, the extensive write-up by Pecharsky and Zavalij⁷ is a good reference. Powder diffraction is one of the most commonly employed techniques to study crystalline materials and compounds. Due to the periodicity and symmetry of atoms and molecules in a crystal, and their interaction with X-rays and neutrons, it is a powerful tool for identifying the average structure. A powdered crystalline sample consists typically of a large number of individual smaller crystallites with sizes on the nm- to μm -scale, ideally

randomly oriented toward the incoming X-rays or neutrons, resulting in a representation of all the diffracting planes in the observed pattern. The basis for the principle of powder diffraction is the combination of elastic scattering (conservation of energy) from atoms of incoming radiation, known as coherent scattering, and Bragg's law³⁸ (Equation 1). Depending on the interplanar spacing between different crystallographic planes in a crystal structure, the scattered waves can either interact constructively or destructively, resulting in a diffraction pattern. This occurs when the wavelength of the incoming radiation is similar to the interatomic distances in the crystal.

$$n\lambda = 2d_{hkl}\sin\theta \quad (1)$$

In Bragg's law, n is an integer ≥ 1 , λ is the wavelength of the incoming radiation, d_{hkl} is the interplanar spacing and θ is the scattering angle. Worth noting is that the measured scattering angle (or angle of diffraction) is 2θ . In the term d_{hkl} , hkl denotes the so-called Miller indices. These are used to index a set of planes, where hkl are the reciprocal numbers of the coordinates where a specific plane intercepts the unit cell vectors. As such, each reflection arising in a diffraction pattern can be attributed to the different crystallographic planes in the crystal structures and are similarly denoted by the respective Miller indices. Utilizing Bragg's law and the measured 2θ angle, d_{hkl} values can be retrieved and used to further determine the unit cell parameters and symmetry of the crystal structure. The integrated intensity, I , of a specific reflection depends on the scattering properties of the atomic species contributing to the reflection and is linked to the structure factor, F_{hkl} , as shown in Equation 2. The structure factor (omitting absorption and multiplicity) is given by Equation 3.

$$I \propto |F_{hkl}|^2 \quad (2)$$

$$F_{hkl} = \sum_{j=1}^n g_j t_j f_j e^{2\pi i(hx_j + ky_j + lz_j)} \quad (3)$$

Here, n is the total number of atoms in the unit cell, g_j is the site occupancy, t_j is the displacement parameter (from thermal vibrations and atomic positional disorder), f_j is the atomic scattering factor and x_j , y_j and z_j are the fractional coordinates indicating the position in the unit cell of the j^{th} atom. The mechanism of scattering differs when using X-rays and neutrons, where the scattering occurs from interactions with the electrons and the nucleus, respectively. This will have an effect on the atomic scattering factor, or atomic scattering length (b_j), which is the term used for neutrons, when comparing the two sources of radiation. With X-rays, since the scattering occurs via electrons, the atomic scattering factor will generally increase with the atomic number of the

scattering element. Further, f_j also decreases with the scattering vector length Q , which is a function of the scattering angle θ and the wavelength λ according to Equation 4. With neutrons however, due to scattering occurring from the nucleus, b_j varies randomly across the different elements, while also being independent of Q . This gives rise to unique complementary approaches when combining the two techniques, where especially neutron diffraction can be a powerful tool to study contributions from elements that would be otherwise harder to distinguish using X-ray diffraction. For both $\text{LiNi}_{0.5}\text{Mn}_{1.5}\text{O}_4$ and $\text{Li}_2\text{VO}_2\text{F}$ the unique scattering properties of neutrons can be utilized to study Li in the presence of heavier elements such as V, Ni and Mn, due to the enhanced contrast compared to X-rays. For neutrons, also the scattering contrast between Ni and Mn is greater, making it possible to differentiate between the two elements more easily.

$$Q = \frac{4\pi \sin\theta}{\lambda} \quad (4)$$

The powder diffraction data in this work have been collected from various instruments and sources. Synchrotron X-ray diffraction data were collected in transmission mode using the P02.1 beam line at the Petra III synchrotron in Hamburg, Germany (Paper II and III).³⁹ In house lab X-ray diffraction was performed in Bragg-Brentano mode on a Bruker D8 Twin-Twin diffractometer, utilizing Cu K_α radiation (Paper I) and in transmission mode on a STOE Stadi P diffractometer, utilizing both Cu and Mo K_α radiation (Paper IV). Neutron diffraction data were collected on the time-of-flight neutron diffractometers Polaris and GEM at the ISIS pulsed neutron spallation source at Rutherford Appleton Laboratory, UK (Paper I) and the Echidna high-resolution powder diffractometer at the OPAL reactor in Sydney, Australia (Paper III).⁴⁰⁻⁴²

3.3.2. Structure analysis based on diffraction data

A popular way of analysing powder diffraction data is the Rietveld refinement method.⁴³⁻⁴⁴ In a Rietveld refinement, a crystal structure based on a starting model is refined against an experimentally observed diffraction pattern. The method is based on refining different parameters in the model using a least squares approach to minimize the square sum of the difference between the observed, $y_{obs,i}$, and calculated, $y_{calc,i}$, intensities at different steps i , see the expression in Equation 5.⁴⁵

$$\sum (w_i(y_{obs,i} - y_{calc,i})^2) \quad (5)$$

Here, w_i is the weight of the observed intensity, which can be derived from the variance associated with $y_{obs,i}$, expressed as $1/\sigma^2(y_{obs,i})$. Based on the starting model of the structure the calculated intensities are then computed using Equation 6.

$$y_{calc,i} = S \sum_{hkl} |F_{hkl}|^2 \phi Corr_{hkl} + y_{bkg,i} \quad (6)$$

S denotes the scale factor and F_{hkl} is the previously introduced structure factor. ϕ is the profile function used to describe the peak profile at the scattering angle at point i and is often modelled as either a Lorentzian, Gaussian or Pseudo-Voigt (a linear combination of the two former) function. $Corr_{hkl}$ is a correction factor that takes into account various factors and contributions dependent on the instrument and the sample. Sample contributions to $Corr_{hkl}$ includes multiplicity, absorption, Lorentz-polarization factor, and preferred orientation. $y_{bkg,i}$ is the contribution from the background, which has contributions from thermal diffuse scattering, incoherent scattering, inelastic scattering, and sample environment. Rietveld refinements of the diffraction data presented in this thesis were performed using the TOPAS software⁴⁶.

3.3.3. Diffraction peak shape modelling

The resulting Bragg reflections from diffraction are ideally discrete sharp peaks, however, in practice the peaks are broadened due to the instrumental setup and the sample. The peak profile in diffraction is a convolution of the instrumental and sample contributions, such as crystallite size, strain and compositional variations.⁴⁷ As such, the peak profile in diffraction can provide additional structural information if the different contributions to its shape can be separated. If the instrument profile is known, typically determined from a strain-free standard sample containing large crystallites, the sample profile can be obtained from the total peak profile by de-convolution. The purely sample induced profile can then provide information on the crystallite size and unit cell distortions from strain and compositional variation.^{19,48} Broadening from size effects is typically symmetrical while broadening from strain and variations in composition can be symmetrical and asymmetrical.⁴⁹ In Paper III, a separation of the different contributions to the peak profile was carried out in order to provide further insights into structural distortions during phase transitions.^{19,48} A Lorentzian peak profile was used to model broadening contribution from the crystallite size (L), where the full width at half maximum (FWHM, β) varies with θ as shown in Equation 7, where λ is the wavelength.

$$\beta = \frac{\lambda}{L \cos\theta} \quad (7)$$

To model peak broadening originating from strain and/or compositional heterogeneity, a convolution of a symmetrical and an asymmetrical profile was used. Symmetrical broadening was modelled with a Gaussian peak profile with a FWHM varying as a function of θ given by Equation 8, where E is the refined strain parameter.

$$\beta = E \tan\theta \quad (8)$$

The asymmetrical part of the convolution was modelled with an exponential function $f(\theta)$, which is defined in Equation 9. Here, ε_{hkl} is the refined strain parameter and θ is defined in the range $[\theta_{hkl}, +\infty]$ if $\varepsilon_{hkl} > 0$, whereas in the interval $[-\infty, \theta_{hkl}]$ if $\varepsilon_{hkl} < 0$.

$$f(\theta) = \exp\left(-\frac{2\theta - 2\theta_{hkl}}{\varepsilon_{hkl}}\right) \quad (9)$$

The total peak profile could then be obtained from convolution of the symmetrical Lorentzian and Gaussian parts together with the asymmetric exponential function. To obtain the sample-induced peak profile from strain/compositional contributions a convolution of the Gaussian and exponential peak profile functions was performed. Furthermore, a population density function (*pdf*) as a function of 2θ could then be constructed for a certain hkl reflection of a given phase, as shown by Equation 10. Here, \otimes denotes convolution, while E and $f(\theta)$ are given from the refined peak profiles.

$$pdf(2\theta)_{hkl} = \frac{2\sqrt{\ln(2)/\pi}}{E \tan\theta} \exp\left(\frac{-4 \ln(2) (2\theta - 2\theta_{hkl})^2}{(E \tan\theta)^2}\right) \otimes f(\theta) \quad (10)$$

The total population density function, *pdf_t*, accounting for all three intermediate LNMO phases, was then given from the individual *pdf* of each phase and the respective scale factors SF_1 , SF_2 and SF_3 , see Equation 11.

$$pdf_t = SF_1 \cdot pdf(2\theta)_{hkl,1} + SF_2 \cdot pdf(2\theta)_{hkl,2} + SF_3 \cdot pdf(2\theta)_{hkl,3} \quad (11)$$

Due to the structure of LNMO being cubic, the lattice parameter a can be obtained from e.g. the (111) reflection. Moreover, the population density of a , considering all three LNMO phases, was then given by $pdf(2\theta)_{111}$ and conversion of 2θ to a via Bragg's law.

3.3.4. Inductively coupled plasma optical emission spectroscopy

The cationic ratios of the $\text{Li}_x\text{VO}_2\text{F}$ samples were determined with inductively coupled plasma optical emission spectroscopy (ICP-OES). ICP-OES is a technique for determining concentration of atomic species in a solution via ionization and excitation in a plasma. From the characteristic emission wavelength of the excited species, their concentration is derived, usually in the $\mu\text{g-mg/L}$ region. Further information on the use of this technique can be found elsewhere.⁵⁰ When the scattering properties of a certain element are either low or similar compared to one or several other elements, obtaining an accurate refined composition from diffraction data alone can be difficult. In this regard, ICP-OES is a helpful aid when defining reasonable starting site occupancies and constraints for a Rietveld refinement. ICP-OES data can also be used as a validation tool for the plausibility of an obtained refined composition from diffraction data.

4. Results and discussion

4.1. Cationic ordering behaviour in $\text{Li}_x\text{Ni}_{0.5}\text{Mn}_{1.5}\text{O}_4$

$\text{LiNi}_{0.5}\text{Mn}_{1.5}\text{O}_4$ can adopt two different structural configurations, where Ni and Mn are either randomly distributed on the same crystallographic site or split between two separate sites. These two configurations are typically categorized as the disordered and ordered forms of $\text{LiNi}_{0.5}\text{Mn}_{1.5}\text{O}_4$. Disordered LNMO has been found to undergo partial transformation to its ordered form during electrochemical cycling. This was observed already after 10 complete charge and discharge cycles during cycling at a slightly elevated temperature of 55°C. Both forms of LNMO show a sudden and drastic decrease in accessible capacity after prolonged cycling.⁵¹ This effect is more severe when this compound is cycled at elevated temperatures and also occurs earlier for the ordered form compared to the disordered LNMO. The combination of the above observations raises the question of whether the rapid capacity fade is solely a result of cycling the material at high potentials (>4.7 V vs. Li^+/Li) or if it is also dependent on the degree of ordering between Ni and Mn. More specifically, if the failing of disordered LNMO can be linked to a gradual conversion to its ordered form when subjected to prolonged cycling. However, ordering would require transition metal rearrangement, a process which has a high energy barrier. This is reflected in an ordering temperature above 700 °C for the fully lithiated LNMO.^{15,51-53} Considering such a high temperature for Ni and Mn ordering, the observed disorder-order transition during electrochemical cycling suggests that the activation barrier for ordering could vary with the Li content in the material. Thus, the motivation for the work presented in the following section was to investigate the thermal ordering behaviour when Li is removed from the structure. The results presented are a summary of the key findings of Paper I.

4.1.1. Structural characterization of $\text{Li}_x\text{Ni}_{0.5}\text{Mn}_{1.5}\text{O}_4$

Transition metal disordered LNMO was first prepared in its fully lithiated state via thermal treatment and its disordered spinel structure was confirmed via X-ray and neutron diffraction. The ordered form of LNMO can be distinguished from the disordered form through diffraction by the presence of superlattice reflections, resulting from Ni and Mn occupying specific crystallo-

graphic sites. In the ordered form, no NiO_6 octahedra are ever adjacent to another NiO_6 , while in the disordered form, different local Ni environment can exist, potentially resulting in Ni clustering. The ordering between Ni and Mn lowers the overall symmetry of the structure in the ordered form from $Fd\bar{3}m$ to $P4_332$ space group symmetry (Figure 8a-b). The superlattice reflections are more clearly visible in the neutron diffraction data, as shown in the simulated diffraction patterns in Figure 8c-d, due to the enhanced scattering contrast between Ni and Mn, compared to X-rays. The observed diffraction patterns of the prepared disordered LNMO indicated no presence of superlattice reflections and could be indexed and modelled in the $Fd\bar{3}m$ space group, as shown in Figure 9. The Ni and Mn occupancies were refined to 0.2318(4) and 0.7682(4), respectively, resulting in the overall composition $\text{LiNi}_{0.46}\text{Mn}_{1.54}\text{O}_4$. A minor presence of the rock-salt impurity phases $\text{Li}_{0.4}\text{Ni}_{1.6}\text{O}_2$ (LNO) and $\text{Li}_{0.05}\text{Mn}_{0.95}\text{O}_2$ (LMO), which are usually formed during annealing⁵³⁻⁵⁴, were found. Various $\text{Li}_x\text{Ni}_{0.46}\text{Mn}_{1.54}\text{O}_4$ ($0 \leq x \leq 1$) samples were then obtained via chemical delithiation and their Li contents were determined via Rietveld refinement. This resulted in a series of six different $\text{Li}_x\text{Ni}_{0.46}\text{Mn}_{1.54}\text{O}_4$ samples with Li compositions $x = 0.000(10)$, 0.222(8), 0.390(9), 0.430(8), 0.520(8) and 0.675(10).

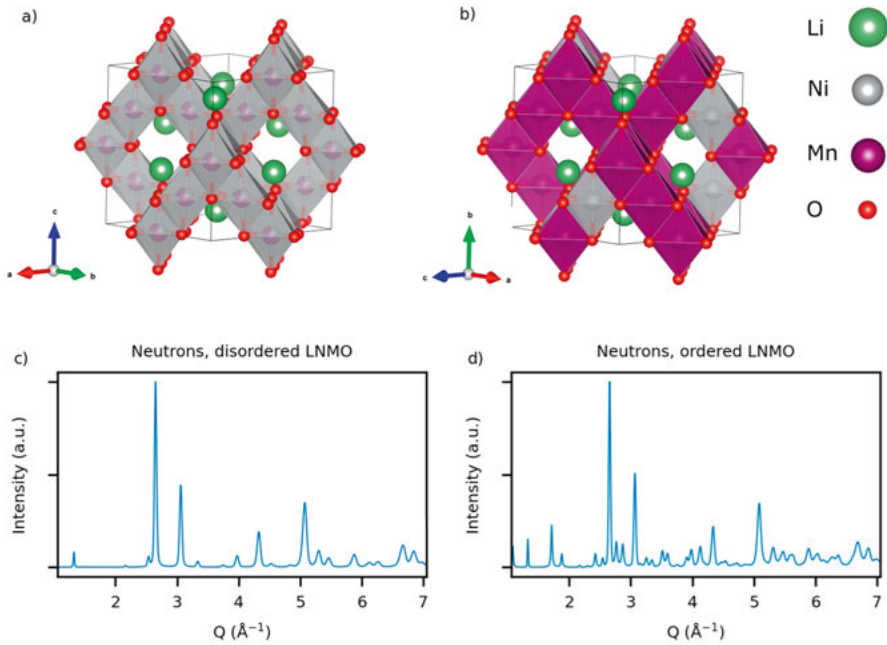


Figure 8. Crystal structures of a) disordered LNMO, space group $Fd\bar{3}m$ and b) ordered LNMO, space group $P4_332$. Simulated neutron diffraction patterns of c) disordered LNMO and d) ordered LNMO.

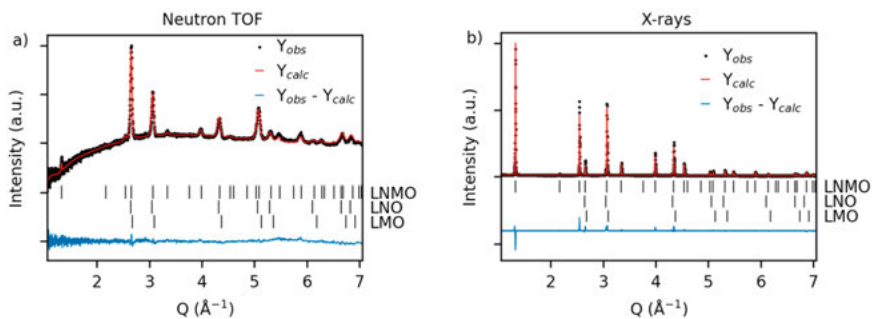


Figure 9. a) Neutron diffraction pattern and b) X-ray diffraction pattern, together with calculated patterns from a Rietveld refinement of cation disordered $\text{LiNi}_{0.46}\text{Mn}_{1.54}\text{O}_4$ (space group $Fd\bar{3}m$).

4.1.2. Structural changes in $\text{Li}_x\text{Ni}_{0.5}\text{Mn}_{1.5}\text{O}_4$ during heating

The chemically delithiated $\text{Li}_x\text{Ni}_{0.46}\text{Mn}_{1.54}\text{O}_4$ samples were studied *in situ* using neutron diffraction during heating. The choice of neutrons over X-rays in this case was made due to the favourable scattering contrast between Li, Ni and Mn, enabling observation of rearrangement of these elements in the structure. During heating of the various $\text{Li}_x\text{Ni}_{0.46}\text{Mn}_{1.54}\text{O}_4$ samples, four principal observations could be made, which will be further detailed and discussed here, exemplified by the results for the $\text{Li}_{0.222(8)}\text{Ni}_{0.46}\text{Mn}_{1.54}\text{O}_4$ and $\text{Li}_{0.430(8)}\text{Ni}_{0.46}\text{Mn}_{1.54}\text{O}_4$ samples.

First, reflections associated with cation ordering could be seen appearing around the temperature 320 °C (Figure 10) for all samples with a Li composition of $0.222(8) \leq x \leq 0.675(10)$. This temperature is significantly lower than the temperature at which ordering occurs in the fully lithiated form of LNMO (>700 °C).^{15,51-53} Only the sample with a Li composition of $x = 0.000(10)$ did not show the same behaviour as it decomposed at around 310 °C. The ordering process could be monitored by tracking the change in Ni and Mn occupancy at the 4a octahedral site, which was obtained from Rietveld refinement, see Figure 11. When comparing trends in terms of ordering, it can be seen that $\text{Li}_{0.430(8)}\text{Ni}_{0.46}\text{Mn}_{1.54}\text{O}_4$ almost reaches full ordering, indicated by a Ni occupancy approaching 1 at the 4a octahedral site, while the same occupancy for $\text{Li}_{0.222(8)}\text{Ni}_{0.46}\text{Mn}_{1.54}\text{O}_4$ only reaches around 0.7. Worth noting here is that due to the weaker tendency to order for samples with a Li composition $x < 0.430(8)$, these were heated to a higher temperature, 350 °C, compared to the other samples (320 °C). However, the higher temperature did not result in a higher degree of ordering compared to samples with $x \geq 0.430$. The degree of ordering between these samples was quantitatively determined from the Ni 4a occupancy at a specific time (900 seconds) after each respective onset of ordering (T_{ord}). The resulting Ni 4a occupancy as a function of Li composition is summarised in Figure 12, where samples with $x \geq 0.430(8)$ appear to almost

fully order, while the ordering decreases with the Li content for the samples where $x < 0.430(8)$.

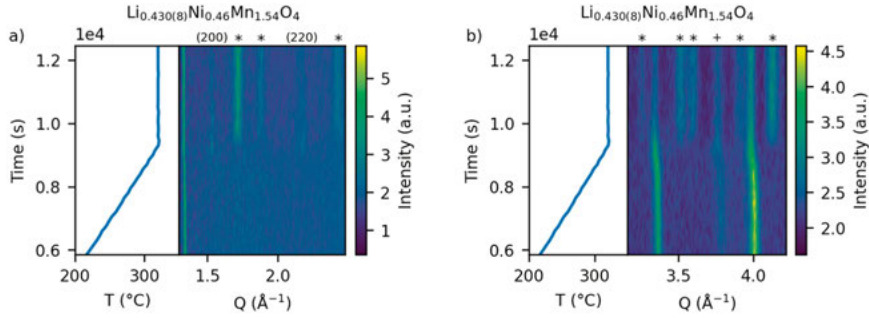


Figure 10. Neutron diffraction contour map of cation disordered $\text{Li}_{0.430(8)}\text{Ni}_{0.46}\text{Mn}_{1.54}\text{O}_4$ during heating, with associated temperature profile, highlighting the Q-regions a) 1.3-2.5 \AA^{-1} and b) 3.15-4.2 \AA^{-1} . Superlattice reflections (*), formation of NiMnO_3 (+) as well as the (200) and (220) reflections are highlighted in the contour map.

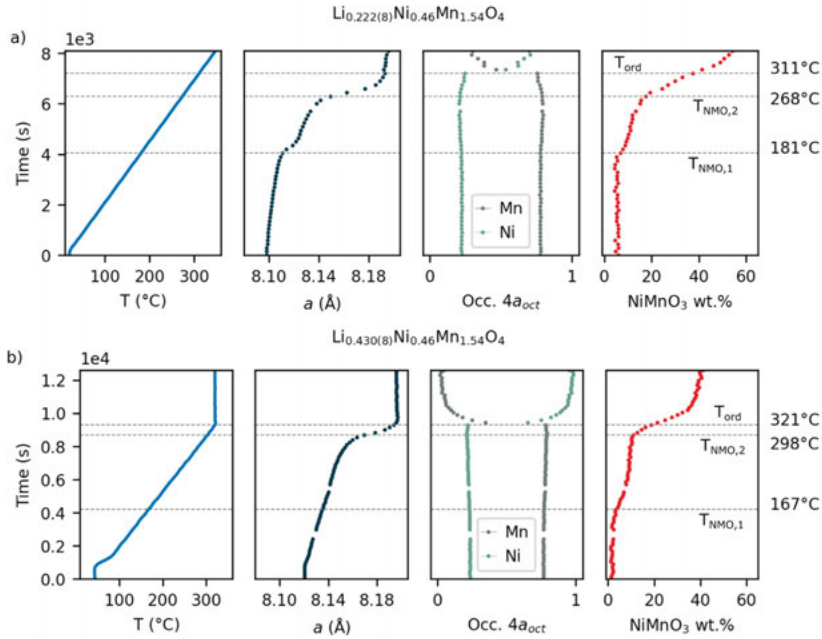


Figure 11. Evolution of structural parameters for a) $\text{Li}_{0.222(8)}\text{Ni}_{0.46}\text{Mn}_{1.54}\text{O}_4$, and b) $\text{Li}_{0.430(8)}\text{Ni}_{0.46}\text{Mn}_{1.54}\text{O}_4$ during heating, obtained from sequential Rietveld refinement. The temperature profile is shown on the left-hand side, followed by the lattice parameter a expressed in \AA , Ni and Mn occupancy at the $4a_{\text{oct}}$ site and weight fraction of the ilmenite-like NiMnO_3 phase. The temperatures for which the phase fraction of the ilmenite-like NiMnO_3 phase begins increasing ($T_{\text{NMO},1}$ and $T_{\text{NMO},2}$) as well as where cation ordering starts (T_{ord}) are highlighted with grey dashed lines.

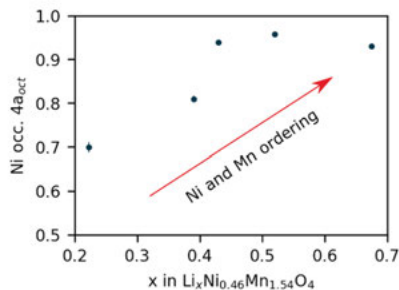


Figure 12. Refined Ni occupancy at the octahedral $4a$ position as a function of Li composition x in $\text{Li}_x\text{Ni}_{0.46}\text{Mn}_{1.54}\text{O}_4$. The Ni occupancy was determined ≈ 900 seconds after ordering was initiated. For the Li composition $x = 0.000(10)$, no transition metal ordering could be observed and as such, the refined occupancy was omitted from this plot.

The second interesting observation was the appearance of intensity in positions corresponding to the (200) and (220) reflections, highlighted in Figure 10a and Figure 13a-b, for samples with a Li composition $0.222(8) \leq x \leq 0.520(8)$. These reflections appeared around or slightly earlier in time compared to the superlattice reflections. The (200) reflection is forbidden in both $R\bar{3}m$ and $P4_332$ symmetry and is shown to be due to Li ordering in the structure, similar to what occurs in LiMn_2O_4 ⁵⁵, which results in a lowering of the symmetry to $P2_13$. From computational studies on LNMO, such a configuration of Li was also found to be the most stable, with similar results for compositions with $\text{Li} < 0.5$.⁵⁶ In the $P2_13$ space group symmetry this Li ordering is manifested by Li occupying a single $4a$ tetrahedral site (Figure 13c), as compared to occupying an $8c$ tetrahedral site in $P4_332$ symmetry. The increasing intensity of the (220) reflection, on the other hand, indicated transition metal rearrangement to tetrahedral sites, analogous to the NiMn_2O_4 spinel structure, and was found to be due to mainly Mn diffusion.⁵⁷ The structure of $\text{Li}_{0.430(8)}\text{Ni}_{0.46}\text{Mn}_{1.54}\text{O}_4$ at 320°C , refined in $P2_13$ symmetry, is shown in Figure 13c. As the Li content decreased from $x = 0.520(8)$ to $0.222(8)$, the refined Mn occupancy at the tetrahedral position increased (Figure 13d), signalling increasing Mn diffusion.

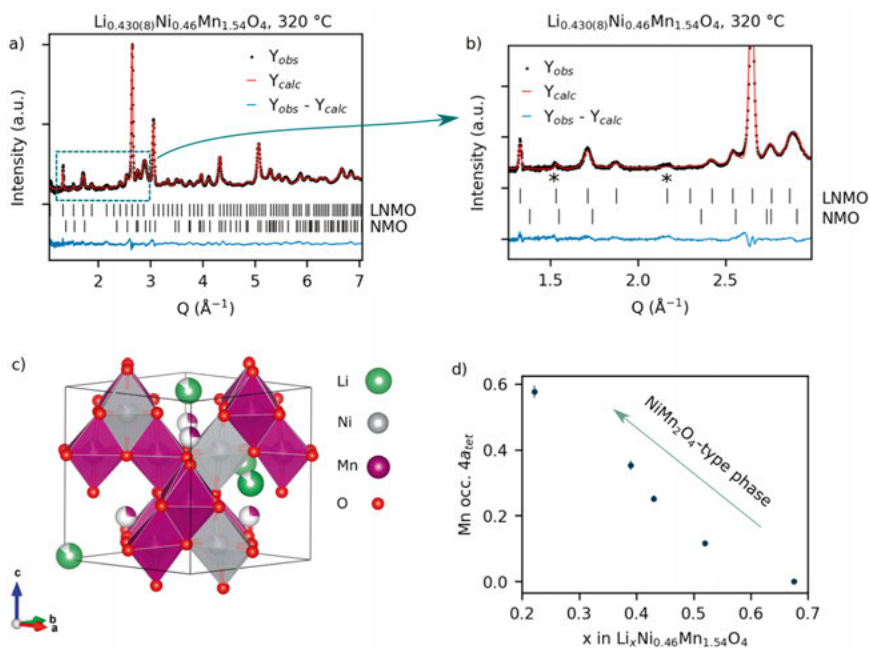


Figure 13. a-b) Neutron diffraction together with the calculated pattern from Rietveld refinement of $\text{Li}_{0.430(8)}\text{Ni}_{0.46}\text{Mn}_{1.54}\text{O}_4$ at 320 °C (space group $P2_13$) with the (200) and (220) reflections highlighted (*), c) visual representation of the refined unit cell in $P2_13$ symmetry and d) refined occupancy of Mn at the $4a_{\text{tet}}$ position as a function of Li content x in $\text{Li}_x\text{Ni}_{0.46}\text{Mn}_{1.54}\text{O}_4$ at $T \geq 320$ °C.

The third observation from the *in situ* neutron diffraction data was the formation of an ilmenite-like NiMnO_3 (NMO) phase, indicated by observed intensity at $Q \approx 3.8 \text{ \AA}^{-1}$ (Figure 10b), which has been found to form during heating of fully delithiated LNMO.⁵⁴ The growth of NiMnO_3 occurred in two steps for all samples at temperatures below 320 °C, exemplified by the $\text{Li}_{0.222(8)}\text{Ni}_{0.46}\text{Mn}_{1.54}\text{O}_4$ and $\text{Li}_{0.430(8)}\text{Ni}_{0.46}\text{Mn}_{1.54}\text{O}_4$ samples in Figure 11. The temperatures for the two formation events of NiMnO_3 , $T_{\text{NMO},1}$ and $T_{\text{NMO},2}$, (together with the temperature for Ni and Mn ordering, T_{ord}) for all samples are summarised in Figure 14. The temperature for the initial growth of NiMnO_3 remained virtually the same for all Li compositions (≈ 170 °C), while the second growth step reached a minimum in temperature at $x = 0.222(8)$. The total amount of NiMnO_3 formed was found to increase as the Li content decreased.

The final noteworthy observation was an expansion of the unit cell, indicated by an increase in the lattice parameter a , which occurred at the same time as the growth of the NiMnO_3 phase, and was most noticeable for the $\text{Li}_{0.222(8)}\text{Ni}_{0.46}\text{Mn}_{1.54}\text{O}_4$ sample (Figure 11a). This unit cell expansion would signal additional structural rearrangements in the $\text{Li}_x\text{Ni}_{0.46}\text{Mn}_{1.54}\text{O}_4$ samples as

the NiMnO_3 phase is formed. In fully delithiated LNMO, this structural reorganization was linked to oxygen release from the structure and a reduction of mainly Ni^{4+} toward Ni^{2+} , resulting in an increase of the Ni-O bond length.⁵⁴ In addition to oxygen release, a NiMn_2O_4 -like structure was shown to be formed, from the diffusion of mainly Mn to tetrahedral sites.⁵⁴

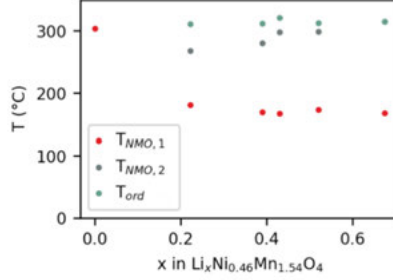


Figure 14. Temperature for the two NiMnO_3 -formation events ($T_{NMO,1}$ and $T_{NMO,2}$) and transition metal ordering (T_{ord}) as a function of Li composition x in $\text{Li}_x\text{Ni}_{0.46}\text{Mn}_{1.54}\text{O}_4$.

4.1.3. Linking structural changes to cation rearrangement in $\text{Li}_x\text{Ni}_{0.5}\text{Mn}_{1.5}\text{O}_4$

All observations mentioned in the previous section can be linked to the rearrangement of cations in the spinel LNMO structure. To better understand the structural reorganization process, transition metal rearrangement across different $\text{Li}_x\text{Ni}_{0.5}\text{Mn}_{1.5}\text{O}_4$ compositions was investigated using density functional theory (DFT) simulations. The resulting energy cost of transition metal displacement to vacant tetrahedral and octahedral sites is summarized in Figure 15. In general, the cost of displacing Mn to both an empty tetrahedral and octahedral site is higher compared to that for displacing Ni across all Li compositions. For a displacement to a tetrahedral site Mn exhibits a parabolic trend, where the energy reaches a minimum at composition for Li x = 0.5. For the octahedral move, Mn exhibits its lowest energy cost at x = 0.375 for Li. However, the energy cost for Mn displacement to the octahedral position across compositions 0-0.5 varies relatively little, compared to the total cost of displacement, spanning values of 3.00-3.35 eV. At a composition for Li x = 1, the energy of the octahedral displacement could not be obtained from the DFT simulations due to difficulties in reaching electric convergence, indicating that the octahedral move has a much higher cost in the fully delithiated state of LNMO compared to when Li-ions are removed from the structure.

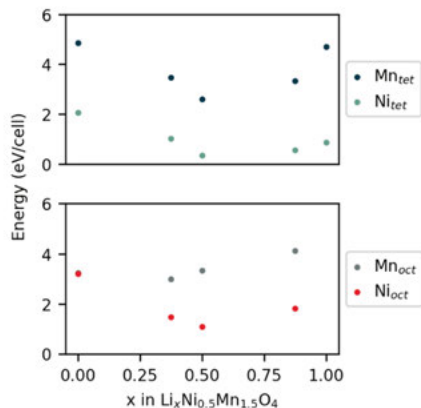


Figure 15. Calculated energies for displacement of Mn and Ni to empty tetrahedral (top) and octahedral (bottom) sites for different Li compositions in $\text{Li}_x\text{Ni}_{0.5}\text{Mn}_{1.5}\text{O}_4$. Note that the energy cost for displacement to an octahedral site at $x = 1$ could not be obtained via DFT due to difficulties in reaching electronic convergence.

The observed lowered temperature for Ni and Mn ordering in the delithiated samples could now be understood from the calculated energy cost for the transition metal diffusion to empty octahedral sites. The mechanism for ordering has been shown to proceed via the formation of Frenkel defects, where Ni and Mn diffuse to vacant neighbouring octahedral positions.¹⁵ As such, the decrease in energy cost for the formation of these Frenkel defects as Li is removed from the structure would explain the lowered temperature of ordering seen from the neutron diffraction data. Since the calculated energy barrier for Frenkel defect formation especially for Mn varies relatively little, compared to the total energy of such a formation, across different Li compositions $x < 0.875$, this results in a similar observed temperature of ordering for the $\text{Li}_x\text{Ni}_{0.5}\text{Mn}_{1.5}\text{O}_4$ samples where $0.222(8) \leq x \leq 0.675(10)$. This result provides some chemical rationale behind the partial transformation of disordered LNMO to its ordered counterpart during electrochemical cycling¹⁴.

The formation of NiMnO_3 - and NiMn_2O_4 -type structures could also be understood by considering the calculated energy costs of the diffusion of transition metals. The NiMnO_3 structure is related to the spinel structure of LNMO, yet with no species occupying any tetrahedral positions. This ilmenite-type structure can be derived from LNMO by moving transition metals to the $16c$ sites and shifting the oxygen stacking sequence from cubic to hexagonal close packing (Figure 16a).⁵⁸ The $16c$ position is analogous to the Frenkel defect sites occupied during the ordering process. Therefore, NiMnO_3 can be formed via a process similar to the Ni and Mn ordering in LNMO, namely via transition metal diffusion to empty octahedral sites, in addition to oxygen loss. Since oxygen release is favoured by the presence of Ni^{4+} , more NiMnO_3 forms as

the Li content decreases. This further explains why NiMnO_3 is not created during ordering in fully lithiated LNMO, since nickel is already in the 2+ state. The influence of the energy barrier for Mn displacement to an octahedral site was reflected in the value of $T_{\text{NMO},2}$, which reached a minimum for the Li composition $x = 0.222(8)$, following a similar trend as the energy cost for the Mn move to an empty octahedral site.

As mentioned previously, diffusion of Mn into tetrahedral sites would lead to a configuration similar to a NiMn_2O_4 -type spinel structure, which has been shown to form in fully delithiated LNMO.⁵⁴ The NiMn_2O_4 spinel structure is similar to LNMO, but instead of being occupied by Li, the tetrahedral sites are populated by transition metals (Figure 16b).⁵⁹ Thus, a NiMn_2O_4 -type spinel can be formed by transition metal diffusion to tetrahedral sites in LNMO. The energy cost associated with such a move could be seen to decrease as Li was removed from the structure between Li compositions $x = 0.5 - 1.0$. A decrease in the energy barrier for Mn displacement onto tetrahedral sites could then explain the observed increase in the refined occupancy of Mn at the 4a tetrahedral position between a Li composition $x = 0.675(10)$ to $0.430(8)$. The calculated energy barrier for the Mn move to a tetrahedral site was found to increase when the Li content dropped below $x = 0.375$, in contrast to the observed continued increase in Mn occupancy at this site. This contradiction could be explained from the ordering process, which raises the energy barrier for Ni and Mn rearrangement and occurs simultaneously.^{15,54} Hence, the observed increased ordering in the samples with Li composition $0.390(9) \leq x \leq 0.675(10)$, compared to the $x = 0.222(8)$ and $0.390(9)$ samples, results in a relatively larger increase in the energy cost for Mn displacement to tetrahedral sites and consequently, in a lower Mn occupancy for the 4a tetrahedral site.

To summarize, the growth of both the NiMn_2O_4 - and NiMnO_3 -type phases was found to increase as the Li content decreased across the compositions $0.222(8) \leq x \leq 0.675(10)$. Additionally, the degree of ordering was found to decrease in the compositional range $0.222(8) \leq x \leq 0.390(9)$. Therefore, all three processes appeared to be in competition with each other, based on a similar mechanism of formation involving rearrangement of transition metals to empty tetrahedral and octahedral sites. This competition is manifested through an increased degree of ordering reducing the formation of NiMn_2O_4 - and NiMnO_3 -type phases at high Li content, and vice versa for low Li content. Both formation of secondary phases and the reorganization to the ordered form can be seen as disadvantageous from an electrochemical performance perspective. If the secondary phases are electrochemically inactive, their formation will result in a loss of capacity. Further, the ordering of Ni and Mn in the structure results in a worsened rate capability of the material, due to the lower Li-ion diffusivity of the ordered form. Therefore, controlling the transition metal diffusion in disordered LNMO is important for minimising loss of capacity and rate capability.

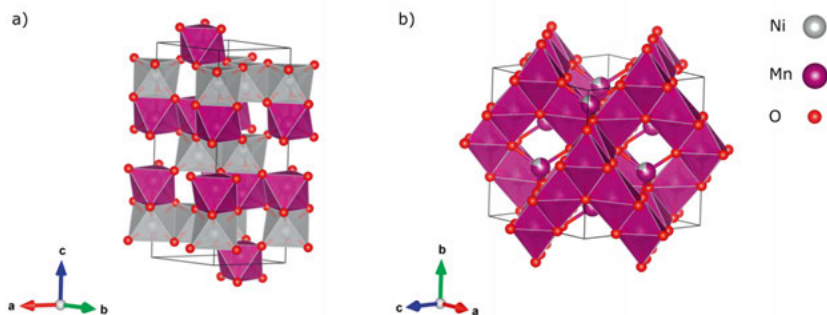


Figure 16. Crystal structure of a) NiMnO_3 , space group $R\bar{3}$ and b) NiMn_2O_4 , space group $Fd\bar{3}m$.

4.2. Phase transition mechanisms in $\text{LiNi}_{0.5}\text{Mn}_{1.5}\text{O}_4$ during electrochemical cycling

Following the establishment of a thermodynamical rationale for the ordering behaviour in $\text{Li}_x\text{Ni}_{0.5}\text{Mn}_{1.5}\text{O}_4$ during cycling, the influence of such ordering on the phase transitions in LNMO was the interest of further work. More specifically, differences in structural transitions during cycling as a function of the degree of ordering in the material. However, prior to conducting measurements, a suitable setup for such a characterization approach needed to be defined. The influence of phase transition mechanisms on the reported differences in rate capability of disordered and ordered LNMO¹⁶⁻¹⁷ has not been studied to a greater extent so far and remains a point of interest. Further, as highlighted earlier in the introduction chapter, interesting structural behaviour involving non-equilibrium phases or phase transitions can occur in battery materials when cycled at high rates. Therefore, the *operando* X-ray diffraction setup specifically targeted high cycling rate studies. The work presented in Paper II revolves around the design and operation of this *operando* setup.

4.2.1. The *operando* pouch cell holder

The motivation for the holder design focuses on utilizing a standard pouch cell, as shown in Figure 7b, in combination with a controlled stack pressure given by a holder. Stack pressure is an often overlooked parameter in different cell designs used for *operando* X-ray diffraction measurements, where an uneven or low stack pressure can result in inhomogeneous reactions in an electrode.²⁸ As a consequence of such inhomogeneity, often the structural transformations occurring in the region probed by the beam are not representative of the macroscopic electrochemical behaviour. In the design presented in this work, hereby referred to as the ‘*operando* pouch cell holder’, a pouch cell is

sandwiched in between two glassy carbon windows in a dedicated frame where the stack pressure is applied and controlled using a wave spring, see Figure 17.

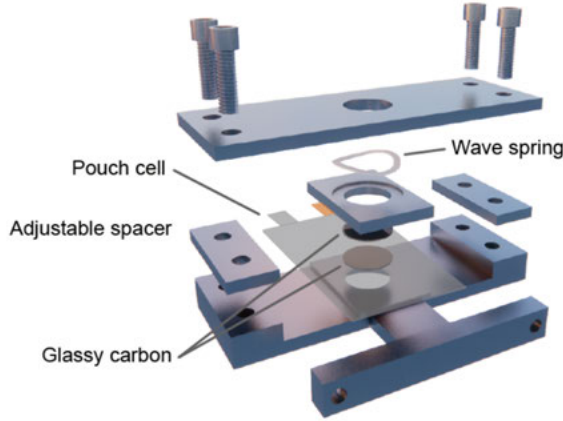


Figure 17. Design and principal sketch of the *operando* pouch cell holder.

The compression length of the wave spring is set by a pair of interchangeable spacers, which can be altered to achieve a certain applied stack pressure. The applied stack pressure, P , can be calculated using the spring constant, k , of the wave spring, the compression length, Δl , and the area of the active material electrode, $A_{electrode}$, as shown by Equation 12. The applied stack pressure used in this work was 0.53 MPa.

$$P = \frac{k \cdot \Delta l}{A_{electrode}} \quad (12)$$

The glassy carbon windows were selected to provide mechanical rigidity and an easily modelled background in the collected diffraction patterns, see Figure 18a. Homogeneity in the applied stack pressure can be assumed based on the flat compression area in combination with the rigidity of the windows. Other window materials such as Be, diamond or sapphire could also be utilized based on the specialized needs regarding either the X-ray energy, or the material as well as the cell chemistry studied using the holder. Apart from the glassy carbon, the inactive materials in the pouch cell, such as Al and the polymer separator, also contribute to the diffraction patterns, as seen in Figure 18b. These contributions could be modelled and accounted for during Rietveld refinements in TOPAS.

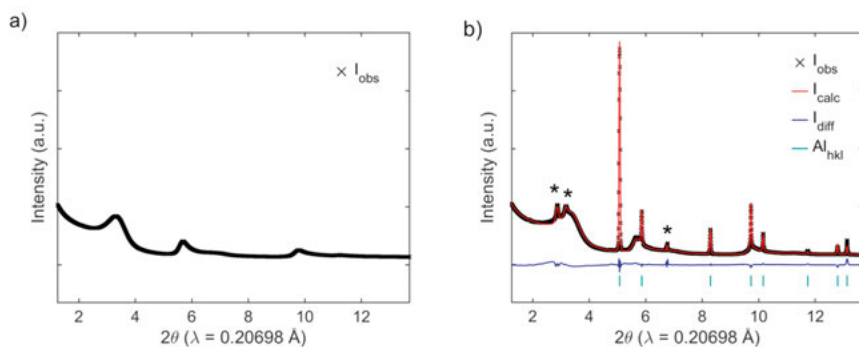


Figure 18. a) Observed X-ray diffraction pattern of the glassy carbon windows. b) Observed and calculated X-ray diffraction patterns of a pouch cell in the holder, without any active material, i.e. $\text{LiNi}_{0.5}\text{Mn}_{1.5}\text{O}_4$. The peaks indicated with * stem from the polymer separator.

To further exemplify the modelling process including all inactive materials, a pouch cell with $\text{LiNi}_{0.5}\text{Mn}_{1.5}\text{O}_4$ as the active material was assembled in the *operando* pouch cell holder and synchrotron X-ray diffraction data were collected. The data was collected on the P02.1 beam line at the Petra III synchrotron, using a wavelength of 0.20698 \AA (roughly 60 keV) and a collection time of 10 seconds. The resulting diffraction pattern and calculated pattern from Rietveld refinement are shown in Figure 19. After accounting for the contributions from glassy carbon, Al and polymer separator, the contribution from $\text{LiNi}_{0.5}\text{Mn}_{1.5}\text{O}_4$ could be modelled successfully.

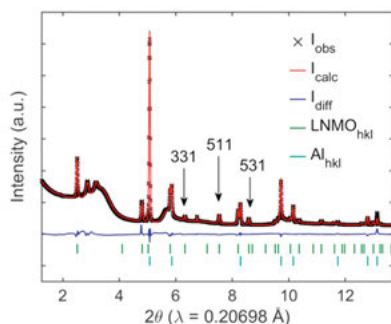


Figure 19. Observed and calculated X-ray diffraction patterns from Rietveld refinement of a pouch cell containing active material, i.e. $\text{LiNi}_{0.5}\text{Mn}_{1.5}\text{O}_4$, in the holder. The (311), (511) and (531) reflections are indicated with arrows.

The electrochemical performance of a pouch cell cycled in the *operando* holder compared to when it is cycled in a standard in-house setup, were found to be similar when considering the measured voltage profiles and capacities,

see Figure 20. If the mass loading is very low, any differences in internal resistance will not be easily noticed in the voltage profile. Here, the two pouch cells were identical, with a resulting mass loading on the cathode of $\approx 5 \text{ mg cm}^{-2}$, which is in the lower range of mass loadings used in commercial cells, and in the range of typical mass loadings used for lab scale cells.⁶⁰ As such, any significant differences in ohmic polarisation between the two cells can be expected to be observed. Even at a relatively high rate of 8C, the cell in the *operando* setup did not exhibit a more prominent polarisation or a lower capacity compared to the reference pouch cell. This indicated that the *operando* pouch cell holder could perform as well as a standardized electrochemical cell, thus making the setup viable for performing studies at high C-rates.

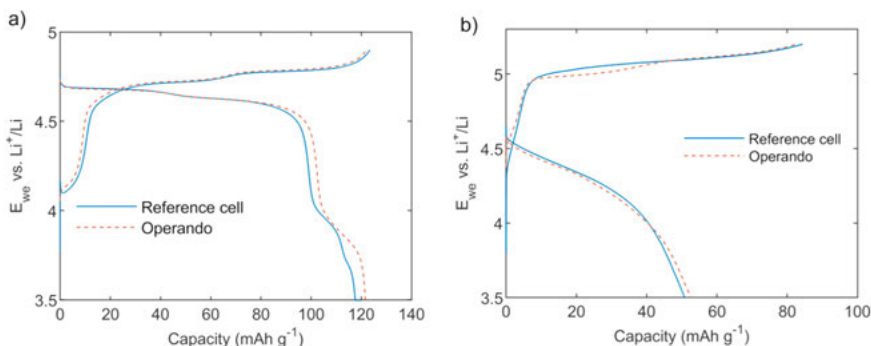


Figure 20. Voltage profiles for galvanostatic cycling at respective rates of a) 1C and b) 8C of a reference pouch cell cycled in house and a cell cycled in the *operando* pouch cell holder.

With a dedicated *operando* cell suitable for X-ray diffraction studies, differences in the structural behaviour of disordered and ordered LNMO during electrochemical cycling could now be studied. While the type of phase transitions in both structural configurations of LNMO are well studied, not much is known about the dynamics of the transitions and how they progress at the particle or crystallite level. Additionally, the first-order phase transitions in ordered LNMO have been found to partially move toward a solid solution-type reaction at elevated rates.⁶¹ A similar observation has been made for LFP, where the two-phase transition could be bypassed in favour of a solid solution reaction at increased rate.¹⁹ Hence, there is additional interest in studying how the phase transition mechanism might change as a function of cycling rate for LNMO. Adding to this, a survey of whether the nature of the phase transition also changes as a function of cation order is of interest and could help shed light on the role of Ni and Mn ordering in determining the rate capability in LNMO. Moreover, in both LNMO and LFP, the previously mentioned transition from two-phase to solid solution did not result in a complete bulk solid

solution spanning the entire Li compositional range. Instead, a metastable decrease in the unit cell mismatch, also known as the miscibility gap, between the respective phases involved in the transition was observed.^{19,48,61} For LFP, this could be explained through the phase transition mechanism at the particle level, and was assessed by careful analysis of the diffraction peak profile.¹⁹ The aim was then to conduct a similar analysis on LNMO to unravel the underlying mechanism of the phase transitions, which is the subject of the work presented in Paper III.

4.2.2. Characterization of the degree of Ni and Mn ordering

Following heat treatment at different annealing times and cooling rates, three LNMO samples with varying degrees of ordering were prepared, resulting in a disordered sample (d-LNMO), an ordered sample (o-LNMO) and a less ordered sample (lo-LNMO), respectively. Characterization of the structure was performed via X-ray and neutron diffraction. The d-LNMO sample could be indexed and modelled in $Fd\bar{3}m$ space group symmetry, see Figure 21a-b, with a resulting composition $\text{LiNi}_{0.44}\text{Mn}_{1.56}\text{O}_4$. The two ordered samples were indexed and modelled in the $P4_332$ space group, see Figure 21c-f. In both ordered samples, the characteristic superlattice reflections were mainly present in the neutron diffraction patterns. Some differences in the relative intensities of these reflections, with respect to those reflections arising from the main spinel framework, could be seen between the two ordered samples, indicating differing degrees of transition metal ordering. From the refined Ni occupancy at the $4b$ site, the degree of ordering could be determined, where an occupancy of 0.2189 and 0.8756 would respectively correspond to 0% and 100% ordering. The degree of ordering was determined to be 87.3(5)% for lo-LNMO and 99.5(5)% for o-LNMO.

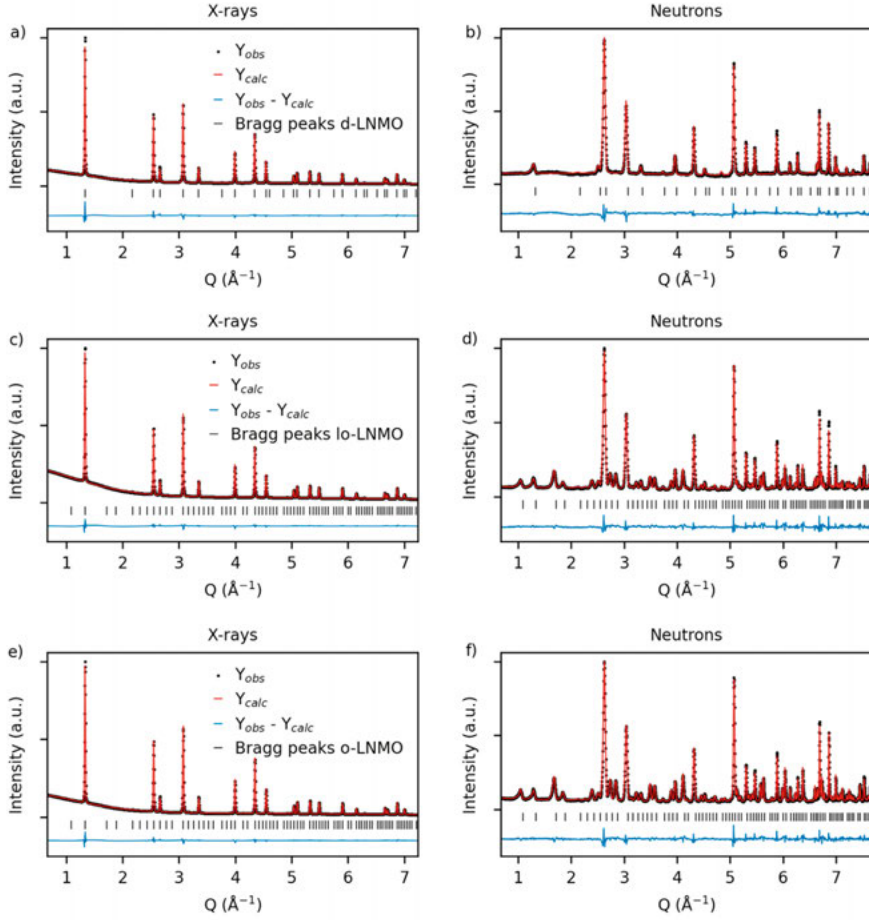


Figure 21. Observed and calculated diffraction patterns from a combined Rietveld refinement of X-ray and neutron diffraction data for a-b) disordered $\text{LiNi}_{0.44}\text{Mn}_{1.56}\text{O}_4$ (d-LNMO), space group $Fd\bar{3}m$, c-d) less ordered $\text{LiNi}_{0.44}\text{Mn}_{1.56}\text{O}_4$ (lo-LNMO), space group $P4_332$ and e-f) ordered $\text{LiNi}_{0.44}\text{Mn}_{1.56}\text{O}_4$ (o-LNMO), space group $P4_332$.

4.2.3. *Operando* X-ray diffraction

The three prepared samples of LNMO were used in the preparation of composite electrodes, which were further assembled into pouch cells for *operando* X-ray diffraction characterization. The results are summarised in Figure 22, where the change in Q of the (531) reflection can be followed during galvanostatic cycling at 1C and 5C for all samples. The characteristic solid solution reaction for the composition $\text{Li}_{1-\delta}\text{Ni}_{0.44}\text{Mn}_{1.56}\text{O}_4$ (where typically, $0 \leq \delta \leq 0.5$) could be observed for the disordered sample, indicated by a continuous shift in Q of the reflection. The solid solution reaction was then followed by a first-order phase transition between $\text{Li}_{1-\delta}\text{Ni}_{0.44}\text{Mn}_{1.56}\text{O}_4$ ($\delta \approx 0.5$) and $\text{Ni}_{0.44}\text{Mn}_{1.56}\text{O}_4$.

(Li₀, Phase III), which is characterized by a discontinuity in the shift of Q between Li_{1-δ}Ni_{0.44}Mn_{1.56}O₄ and Phase III. For the two ordered samples, the two separate first-order phase transitions between intermediate phases LiNi_{0.44}Mn_{1.56}O₄ (Li₁, Phase I) and Li_{0.5}Ni_{0.44}Mn_{1.56}O₄ (Li_{0.5}, Phase II) and Phase II/Phase III could also be identified from discontinuities in the shift of Q for the (531) reflection.

When comparing the two ordered samples, the reflection associated with Phase I in lo-LNMO was found to extend toward higher values of Q, compared to for o-LNMO. This would indicate that the unit cell mismatch, or miscibility gap, between Phase I and Phase II was reduced for lo-LNMO, possibly due to the appearance of a solid solution Li_{1-δ'}Ni_{0.44}Mn_{1.56}O₄ ($0 \leq \delta' < 0.5$).

Another interesting observation that could be made for all samples was that peak broadening occurred when the rate was increased from 1C to 5C. Given that the instrumental contribution to any peak broadening does not change between the two rates, the observed broadening must originate from the sample.⁴⁷ Further, it was found that the broadening was not only symmetric, but also exhibited asymmetry. More specifically, reflections from co-existing intermediate phases were found to extend towards each other, pointing toward a reduction in the miscibility gap between the involved phases. Such an asymmetry must be a result of strain and/or compositional variations and cannot be explained by changes in the crystallite/domain size.^{19,48-49}

It should be noted here that Li-ion concentration gradients could be present in the composite electrode as a result of slow kinetics and Li-diffusion in the solid state.^{8,23} Such concentration gradients are typically manifested in the material as a more advanced reaction front at the surface in contact with the electrolyte, as compared to the material closer to the current collector.²³ By considering the diffusion length L as a function of the square root of time, t , and diffusivity, D , following Fick's law, either L or t can be determined (). Using a Li-ion diffusivity of $510^{-9} \text{ cm}^2 \text{ s}^{-1}$,⁶² the calculated Li-ion diffusion time through the thickness of the composite electrodes (10 and 25 μm) was around 100 and 625 seconds, i.e. on a time scale shorter than the galvanostatic cycling employed here (1C-10C). Only for cycling of the thicker electrodes at 5C is the time scale of Li-ion diffusion (625 s) comparable to the time domain of one complete charge or discharge (720 s). As such, inhomogeneity in the reaction state of the electrodes is not expected here, except at 5C. The particle size for the samples (5 μm) does not lie in the region where Li-ion diffusion starts to be limiting at the rates applied here. As such, reaction inhomogeneity in individual particles is not expected. Since X-ray diffraction probes the bulk, it is not possible to distinguish where in the material any inhomogeneities in the progress of the phase transition originate. In the case of a two-phase reaction, such inhomogeneity will be manifested by the presence of diffraction peaks associated with both phases. However, reaction inhomogeneity at the electrode level only affects the relative intensity of the diffraction peaks when

comparing the respective phases and not the peak shape. Therefore, the observed broadening cannot be attributed to reaction inhomogeneities in the electrode.

The broadening behaviour is illustrated in Figure 23, where a fit of the peak profiles with no additional broadening is compared to a fit with added symmetrical and asymmetrical broadening for the ordered sample at around 2/3 state of charge (SOC, $C_{charge} \approx 100 \text{ mAh g}^{-1}$). The fit was significantly improved by the inclusion of added strain broadening in this case. Furthermore, broadening from a decrease in the crystallite size could be ruled out empirically by comparing the fitted peak profiles from size-modelled and strain-modelled broadening. The strain model was shown to result in a better fit of the observed peak profile. This led to the conclusion that broadening was solely due to a variation in the lattice parameters in the sample, caused by strain and/or compositional variations within individual crystallites.

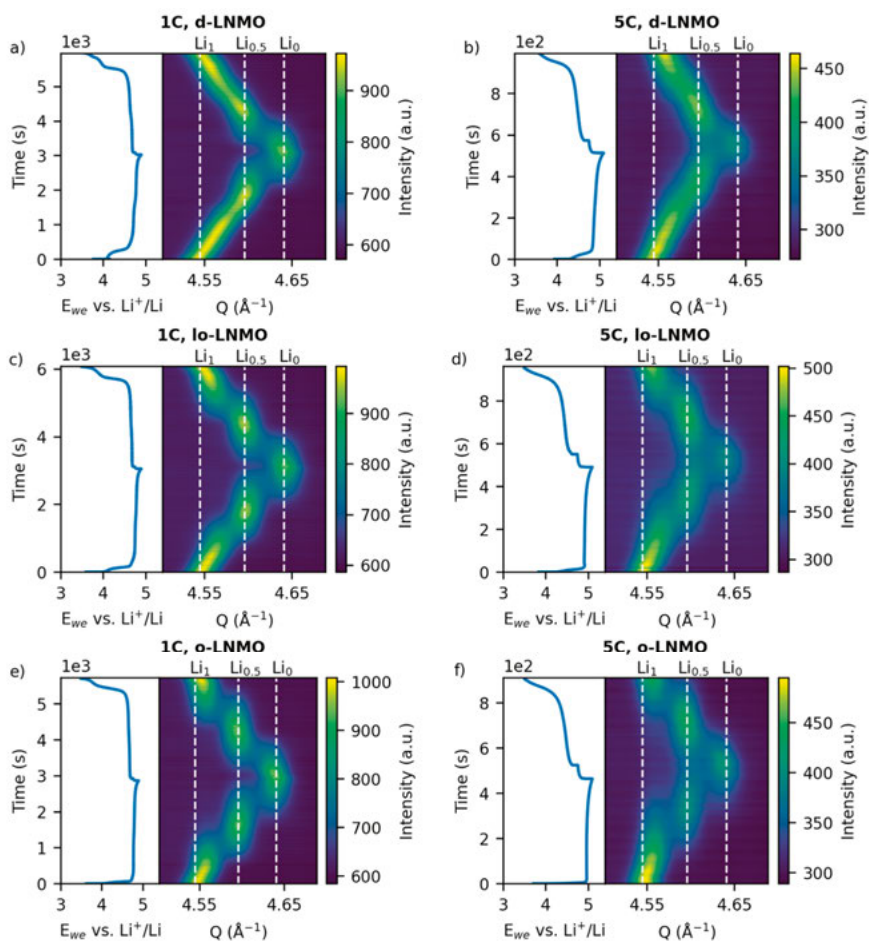


Figure 22. Change in Q of the (531) reflection during galvanostatic cycling at 1C and 5C of a-b) disordered LNMO (d-LNMO), c-d) less ordered LNMO (lo-LNMO) and e-f) ordered LNMO (o-LNMO). The peak positions of the intermediate phases $\text{LiNi}_{0.44}\text{Mn}_{1.56}\text{O}_4$ (Li_1), $\text{Li}_{0.5}\text{Ni}_{0.44}\text{Mn}_{1.56}\text{O}_4$ ($\text{Li}_{0.5}$) and $\text{Ni}_{0.44}\text{Mn}_{1.56}\text{O}_4$ (Li_0) are indicated by the dashed white lines.

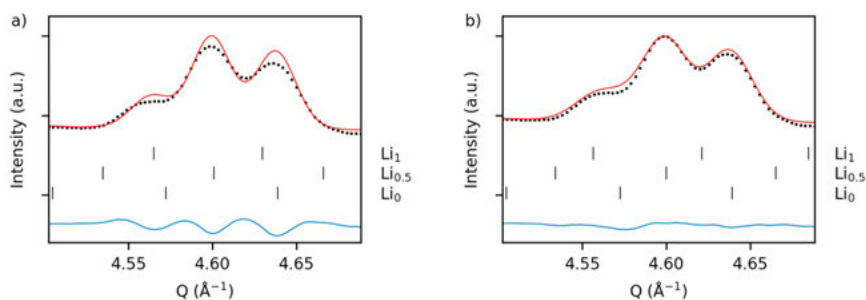


Figure 23. Observed and calculated diffraction patterns of ordered LNMO at the co-existence of the three intermediate phases $\text{LiNi}_{0.44}\text{Mn}_{1.56}\text{O}_4$, $\text{Li}_{0.5}\text{Ni}_{0.44}\text{Mn}_{1.56}\text{O}_4$ and $\text{Ni}_{0.44}\text{Mn}_{1.56}\text{O}_4$ during charge at 5C ($C_{\text{charge}} \approx 100 \text{ mAh g}^{-1}$, 2/3 SOC), with a) no additional broadening and b) added symmetrical and asymmetrical broadening.

4.2.4. Identifying phase transition mechanisms from diffraction

To further understand the different changes in the miscibility gap between the phases in LNMO, the results need to be put in a context of the different mechanisms by which phase transitions may occur during (de)lithiation. More specifically, how these mechanisms can be manifested in the observed peak profile from diffraction. This is summarised and illustrated in Figure 24 for the phase transition between two generic phases, Phase I and Phase II. In the case of a first-order phase transition with co-existing phases within individual particles, symmetric broadening of the peak profile can occur as a result of a decrease in the crystallite size (Figure 24a). If there is coherency at the interphase between the two phases, the structure can distort on both sides of the interphase, leading to an asymmetric distribution of lattice parameters and asymmetric broadening (Figure 24b).¹⁹ Further, if the nucleating phase is in minority within single crystallites, this can result in a larger strain and distortion compared to the parent phase. The result is an asymmetrical broadening of the peak profile associated with the minority phase (Figure 24d).^{48,63} Asymmetrical broadening, similar to the coherent interphase mechanism, can also occur when there are compositional variations within individual crystallites present (Figure 24c). These variations can occur from high-rate induced solid solution reactions, which has been shown for LFP.^{19,64} Note that these compositional variations are different from those arising from limitations in Li-ion diffusion, since a solid solution can have a composition in between that of Phase I and Phase II. Compositional variations arising from limitations in Li-ion diffusion are limited to the composition of either Phase I or Phase II. Since both the coherent interphase and the rate-induced solid solution mechanism produce similar asymmetric broadening, they can be hard to separate merely by peak profile analysis. However, how the broadening occurs with respect to the phases involved can be used to obtain an indication regarding which of the

two mechanisms is more probable, which will be further discussed for the different LNMO samples.

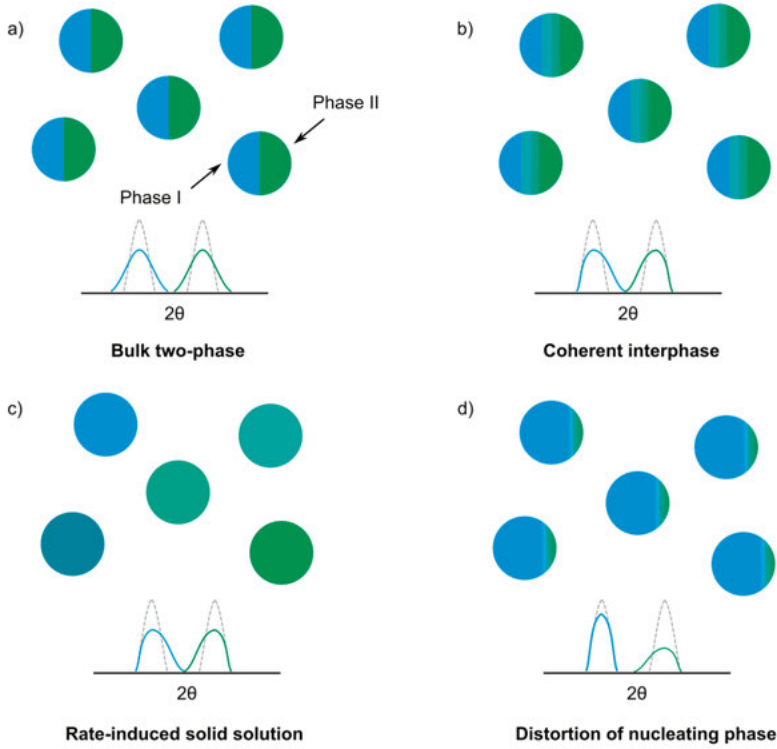


Figure 24. Illustration of different phase transition mechanisms during (de)lithiation; a) bulk two-phase mechanism, b) two-phase mechanism with coherent interphase, c) rate-induced solid solution in individual crystallites and d) distortion of a nucleating phase.

4.2.5. Quantifying changes in the miscibility gap and assessing phase transition mechanisms

The next step was to quantify the distribution of lattice parameters and consequent miscibility gap narrowing. This was done through deconvolution of the different contributions to the diffraction peak profile. Quantification of the lattice parameter distribution was carried out by following the methodology described earlier in Section 3.3.3., where the purely sample-induced peak profile was obtained via convolution of a symmetric strain and asymmetrical strain/compositional peak profile. It was then possible to construct the population density function (*pdf*) which gives a visual representation of the distribution of lattice parameters in the sample. The corresponding lattice parameter

distributions, calculated from the same data sets presented in Figure 22, are presented in Figure 25 and Figure 26.

For d-LNMO, the asymmetric broadening first started to appear during the co-existence of $\text{Li}_{1.8}\text{Ni}_{0.44}\text{Mn}_{1.56}\text{O}_4$ and Phase III. Further, the miscibility gap between these two phases decreased as a result of the lattice parameter distribution widening for both phases symmetrically and asymmetrically toward each other. This would be expected for a mechanism involving a coherent interface, since the interphase only exists in the presence of two phases, which is also in agreement with previous findings on LNMO.⁶¹ Some phase separation could be observed at 5C, specifically between Li compositions $x = 0.5$ -1, which probably was due to the limitations in Li-ion diffusion and resulting reaction inhomogeneity in the composite electrode.²³ Also, when cycling at 5C, to account for the increased ohmic polarisation, the upper voltage cut-off was adjusted to > 5 V at the end of charge, which can lead to electrolyte oxidation.⁶⁵ However, the time spent above 5 V during cycling at 5C is less than 10% of the total charging time for all samples. As such, the influence of electrolyte oxidation is limited to the very end of charge. Further, it appears to have a very small effect on the phase transition in the material, as this can be seen to progress throughout the full charge. When increasing the applied rate from 1C to 5C, the miscibility gap was seen to narrow further. This decrease in the miscibility gap with increasing rate could be understood from the rate-limiting step in LNMO during phase transitions, which is the rearrangement of chemical bonds at the interphase.^{61,66} At high rate, the movement speed of the interphase becomes kinetically limiting.⁶¹ In such a case, a kinetically more favourable solid solution is induced, resulting in a coherent interphase of increased length with an increased population of intermediate lattice parameters between $\text{Li}_{1.8}\text{Ni}_{0.44}\text{Mn}_{1.56}\text{O}_4$ and Phase III.

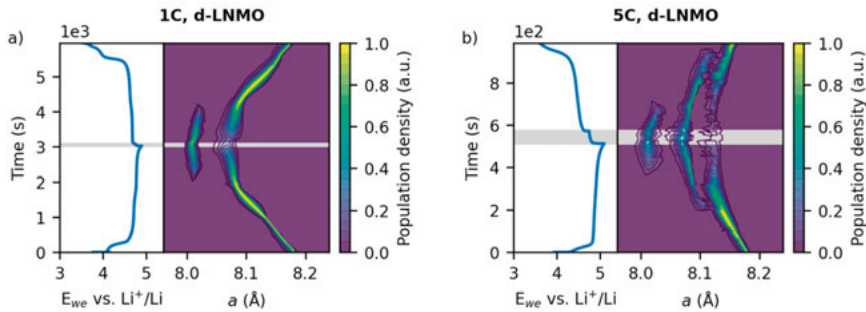


Figure 25. Distribution of the lattice parameter a during galvanostatic cycling at a) 1C and b) 5C of disordered LNMO (d-LNMO), together with associated voltage profiles, respectively. The lowest contour of the population density is drawn at a value of 0.05. The rest period at open-circuit voltage (OCV) is indicated by the shaded grey area.

Looking at lo-LNMO and o-LNMO, asymmetric broadening was also found to occur during the co-existence of two phases, similar to d-LNMO. The lattice parameter distributions of the phases involved in the two first-order phase transitions were also found to extend toward each other. This decrease in the miscibility gap was found to be larger for lo-LNMO, compared to the ordered sample at a similar rate. Further, for both ordered samples, the miscibility gap decreased further with an increasing rate from 1C to 5C. This would again indicate a mechanism involving the formation of a coherent interphase, with a similar relationship between the cycling rate and the movement speed of the interphase at increased rate. The overall smaller miscibility gap for lo-LNMO compared to o-LNMO suggests a coherent interphase of increased length. This could be understood by considering the energy barrier for forming a solid solution in LNMO, which has been shown to be lower when the degree of ordering is decreased.⁶⁷

For lo-LNMO and o-LNMO, the lattice parameter distribution of Phase II appeared wider on charge compared to discharge. This hysteretic behaviour was further investigated by also cycling the ordered samples at 10C, where the hysteretic feature disappeared for lo-LNMO, while remaining to some degree for o-LNMO. This behaviour for the transition involving Phase I and Phase II could be explained when taking into consideration differences in the activation barriers for this process during delithiation and lithiation. The transition from Phase I to Phase II is kinetically faster than the transition between Phase II and Phase III as a result of their respective activation barriers.^{66,68-69} This results in Phase I forming instantly on discharge as the transition to Phase II is completed. While the distribution of lattice parameters for Phase II appears narrow during lithiation, the distribution for Phase I still exhibited asymmetry towards Phase II, as exemplified in Figure 26a. This could be explained by the previously mentioned mechanism involving a distorted minority nucleating phase (Figure 24d), in this case Phase I. Due to the favourable kinetics for the full conversion to Phase I, as soon as Phase I starts growing further, the transition from Phase II is very fast, and the coherent interphase is not maintained. As the rate is increased, the hysteretic behaviour decreased, more so for the less ordered sample. This observation would suggest that the rate of lithiation competes with the faster kinetics of the phase transition on discharge in the material, resulting in the formation of a coherent interphase once again. As such, it appears that the transition metal ordering plays a role in the occurrence of hysteretic behaviour and could possibly be linked to the ability of forming (meta)stable solid solutions.

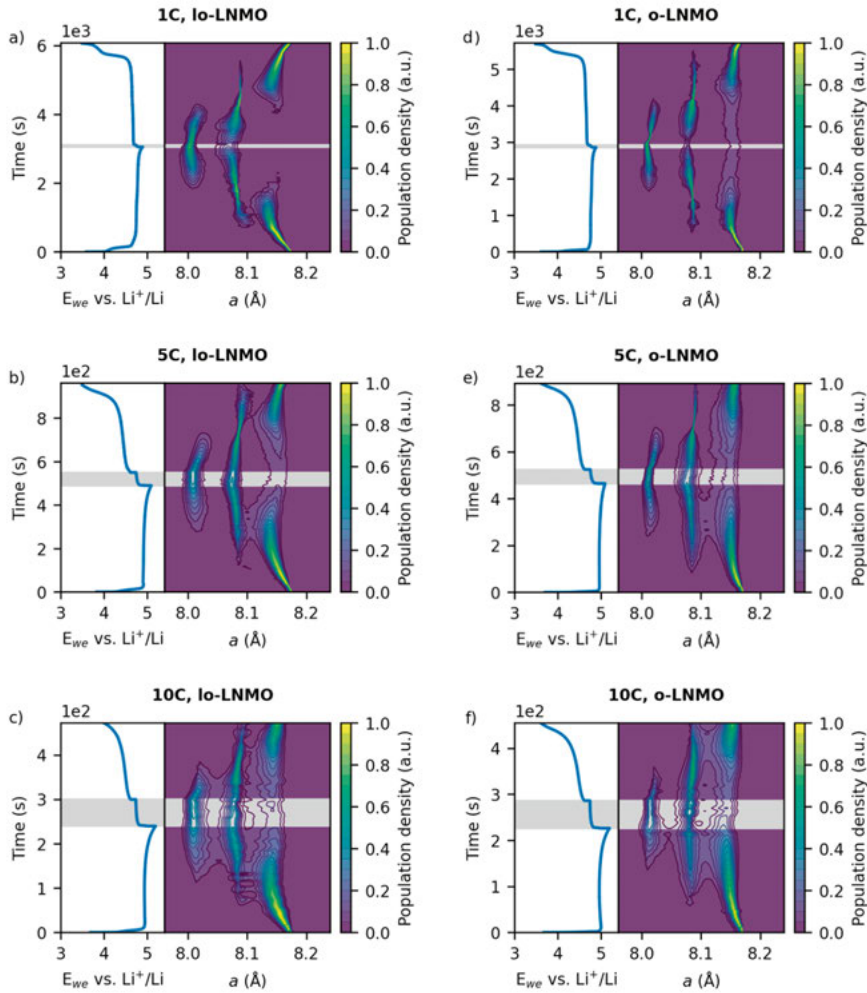


Figure 26. Distribution of the lattice parameter a during galvanostatic cycling at 1C, 5C and 10C, together with associated voltage profiles, respectively, of a-c) less ordered LNMO (lo-LNMO) and d-f) ordered LNMO (o-LNMO). The lowest contour of the population density is drawn at a value of 0.05. The rest period at open-circuit voltage (OCV) is indicated by the shaded grey area.

In summary, the tendency to form a narrower miscibility gap with increasing disorder in LNMO could aid in explaining the reported superior high-rate performance of its disordered form compared to the ordered form. The greater ability to form metastable solid solutions in the disordered form can limit the kinetic influence of a sluggish moving phase transition front, leading to a better rate capability.

4.3. Structural changes in $\text{Li}_2\text{VO}_2\text{F}$ during prolonged electrochemical cycling

Given the insights on how cation arrangement governs both the equilibrium and non-equilibrium structural behaviour in LNMO, the question then arises how cationic organization influences electrochemical performance in other rock-salt derived materials. As mentioned in the introduction, the rock-salt derived class of materials share many structural similarities, where the ordering of cations can determine the structure type. As such, it is of interest to investigate if cation rearrangement also plays a role in the structural transitions of other rock-salt derived structures. Therefore, in Paper IV, the focus was on another type of battery cathode chemistry; the disordered rock-salt $\text{Li}_2\text{VO}_2\text{F}$. The metastable DRS $\text{Li}_2\text{VO}_2\text{F}$ is known to undergo large structural rearrangements during electrochemical cycling, making it an interesting, however complex, material to study. These structural transitions include, but are not limited to, amorphization.²² However, due to the few studies on how the structure changes during prolonged cycling, the role of structural changes in the observed drastic capacity fade remains unknown. Here, the unique complementary characteristics of X-ray and neutron diffraction were utilized to study structural changes in $\text{Li}_2\text{VO}_2\text{F}$ upon chemical delithiation and prolonged galvanostatic cycling. Chemical delithiation was performed on the nanoparticulate powdered sample in solution, as described in Section 3.1.3. The long stirring time in solution (1 week) was chosen as to obtain phases at thermodynamical equilibrium. The work presented here aims at studying if there is a tendency of the metastable DRS structure to convert into thermodynamically stable phases, similar to chemical delithiation, or if other metastable phases are formed. In addition, the role of cation arrangement in structural changes and whether the phases formed can be responsible for the observed capacity fade was explored. Finally, any similarities with the mechanisms involving cationic organisation previously observed in LNMO and in other DRS compounds were investigated.

4.3.1. Structural characterization of $\text{Li}_x\text{VO}_2\text{F}$

Since the scattering strength of V with X-rays is relatively high compared to that of Li, X-ray diffraction is particularly sensitive to the position of V relative to Li in the structure. On the other hand, in neutron diffraction, the scattering from Li is relatively high compared to the almost negligible scattering from V, making the technique suitable for identifying the Li position instead. In contrast, the scattering strength of O and F are relatively similar, both with X-rays and neutrons. The pristine $\text{Li}_2\text{VO}_2\text{F}$ compound could be refined and indexed with the space group $Fm\bar{3}m$, owing to the DRS structure, as shown in Figure 27, in good agreement with previous reports in the literature.³¹ The

diffraction peaks are quite broad which is a feature of the nanocrystalline nature of the material.^{22,52} More details regarding the refined structural parameters for pristine $\text{Li}_2\text{VO}_2\text{F}$ can be found in Paper IV.

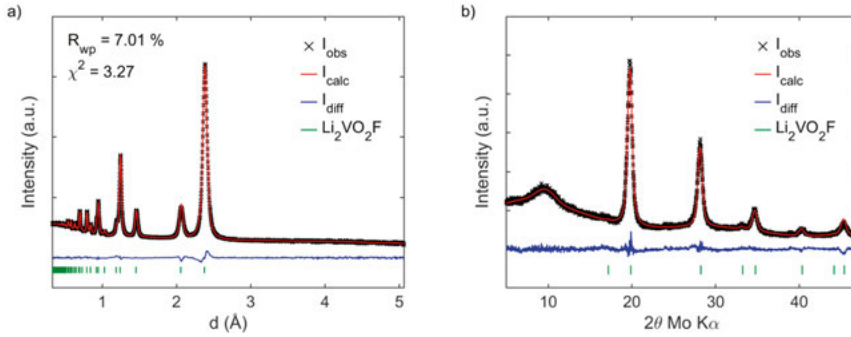


Figure 27. a) Neutron and b) X-ray diffraction patterns and calculated model from Rietveld refinement of pristine $\text{Li}_2\text{VO}_2\text{F}$.

When studying the chemically de-lithiated samples, no new phases or major structural re-arrangements could be observed for the two samples with refined compositions of $\text{Li}_{1.16(1)}\text{VO}_2\text{F}$ and $\text{Li}_{1.107(6)}\text{VO}_2\text{F}$. However, for the most de-lithiated sample with the composition $\text{Li}_{0.783(9)}\text{VO}_2\text{F}$, an additional reflection could be observed from the diffraction data at an interplanar spacing corresponding to $d \approx 4.9 \text{ Å}$, as seen in Figure 28. In studies on the thermal decomposition of $\text{Li}_2\text{VO}_2\text{F}$ and from computational studies, a more thermodynamically stable configuration has been found as a result of phase segregation into layered LiVO_2 (trigonal, $R\bar{3}m$), see Figure 29, and LiF (cubic, $Fm\bar{3}m$).³²⁻³⁴ As such, LiVO_2 was introduced as a second crystalline phase in the refinements for this sample, leading to a successful fit of the additional reflection. This result hints at the role of a high Li content being key to stabilizing the DRS structure of $\text{Li}_2\text{VO}_2\text{F}$ at room temperature.

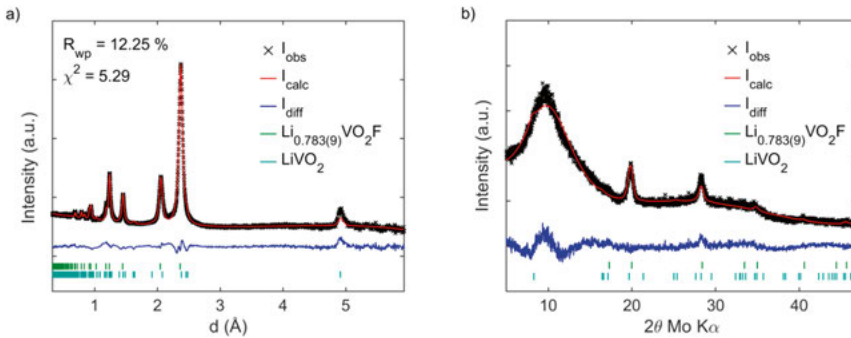


Figure 28. a) Neutron and b) X-ray diffraction patterns and calculated model from Rietveld refinement of chemically delithiated $\text{Li}_x\text{VO}_2\text{F}$, $x = 0.783(9)$.

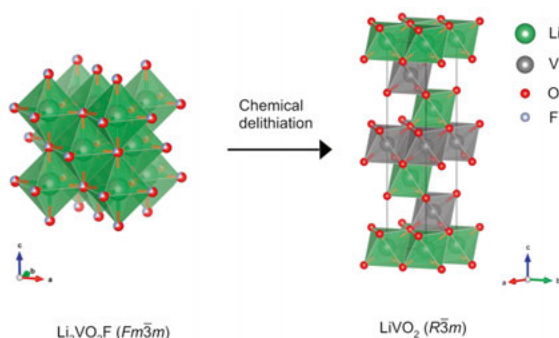


Figure 29. Visual representations of the disordered rock-salt structure of $\text{Li}_2\text{VO}_2\text{F}$ and the layered trigonal LiVO_2 structure.

4.3.2. Prolonged cycling of $\text{Li}_2\text{VO}_2\text{F}$

To study the effects of continuous electrochemical cycling on the structure of $\text{Li}_2\text{VO}_2\text{F}$ and to determine if segregation to thermodynamically stable phases occurs, the material was cycled galvanostatically between 1.3 - 4.1 V vs. Li^+/Li with a C-rate of C/20 ($C_{\text{theoretical}} = 462 \text{ mA g}^{-1}$) for 100 cycles before the diffraction measurements were performed. The electrochemical performance is discussed in Paper IV. Interestingly, in the electrochemically cycled material the appearance of an additional reflection can be noticed in the diffraction data at around $d \approx 4.1 \text{ \AA}$, as seen in Figure 30. This reflection could not be accounted for in the space group $Fm\bar{3}m$, as it is systematically extinct. It could neither be attributed to a phase segregation toward the layered trigonal LiVO_2 (or LiF), contrary to the chemically delithiated sample. The absence of thermodynamically stable phases implies that the material undergoes non-equilibrium transformations during electrochemical cycling, forming additional metastable phases. Since the peak is visible with both X-ray and neutron diffraction, the data suggest that this structural rearrangement or formation of a new phase does not originate from exclusive Li or V ordering. If this was the case, the peak would then only be visible in one of the techniques and not in the other, barring any major re-arrangement of O and F in the structure.

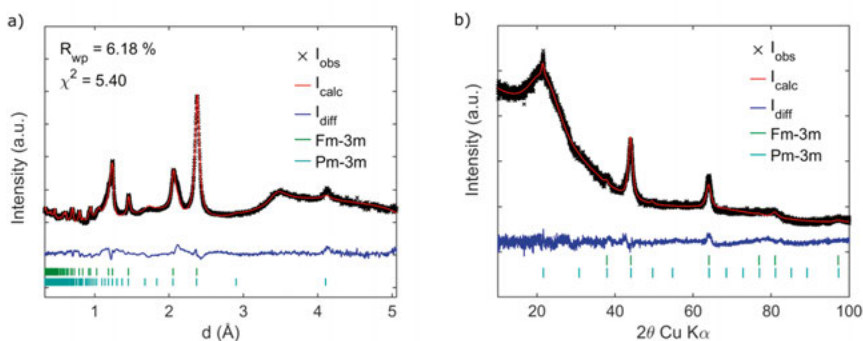


Figure 30. a) Neutron and b) X-ray diffraction patterns and calculated model from Rietveld refinement of $\text{Li}_2\text{VO}_2\text{F}$ after electrochemical cycling, including the additional $\text{Pm}\bar{3}m$ phase.

From previous observations using total scattering, it is known that the DRS structure of $\text{Li}_2\text{VO}_2\text{F}$ undergoes partial amorphization upon electrochemical discharge, forming a pseudo-orthorhombic LiVO_3 -like structural motif.²² A potential match of the observed additional peak to crystalline LiVO_3 was explored, but did not render successful indexing or fitting. Further exploration of possible cation ordering was conducted by considering different known cation-ordered rock-salt structures, such as the γ - and β - LiFeO_2 -type structures.⁷⁰ Neither of these resulted in a satisfying indexing of the reflection seen at around $d \approx 4.1$ Å.

4.3.3. Anionic redox behaviour and cationic reorganization

As it stands right now, no experimental observations of a phase that could explain the results seen in this study exist in the literature. As such, phases predicted by computational modelling in combination with observed structural re-arrangement from Li-rich DRS and layered materials were explored. From density functional theory (DFT) calculations and various experimental techniques, such as transmission electron microscopy (TEM), Raman spectroscopy and resonant inelastic X-ray scattering (RIXS), it is known that both DRS and layered Li-rich compounds undergo anionic redox reactions.^{34,71-78} The anionic redox reactions in these compounds during the delithiation step arise due to the oxidation of oxygen anions in the structure (O^{2-}) and is often accompanied by dimerization to form peroxide, O_2^{2-} , and superoxide, O_2^- , species.^{34,71-78} If the oxidation of these species proceeds further, the result is formation of O_2 molecules, which can lead to loss of oxygen from the structure in the form of oxygen gas. The formed O^{n-} species are stabilized in the structure by a combination of cationic re-arrangement and Li-ion vacancy clustering around the O^{n-} -species. As Li-ions are reinserted in the structure upon discharge, local clusters of highly Li-coordinated oxygen environments are

formed. In the case of a transition metal (TM) based Li-rich DRS oxyfluoride structure, these local clusters would be described as $O(TM_2Li_4)$, $O(TMLi_5)$ and $O(Li_6)$ environments. The full mechanism is illustrated in Figure 31.

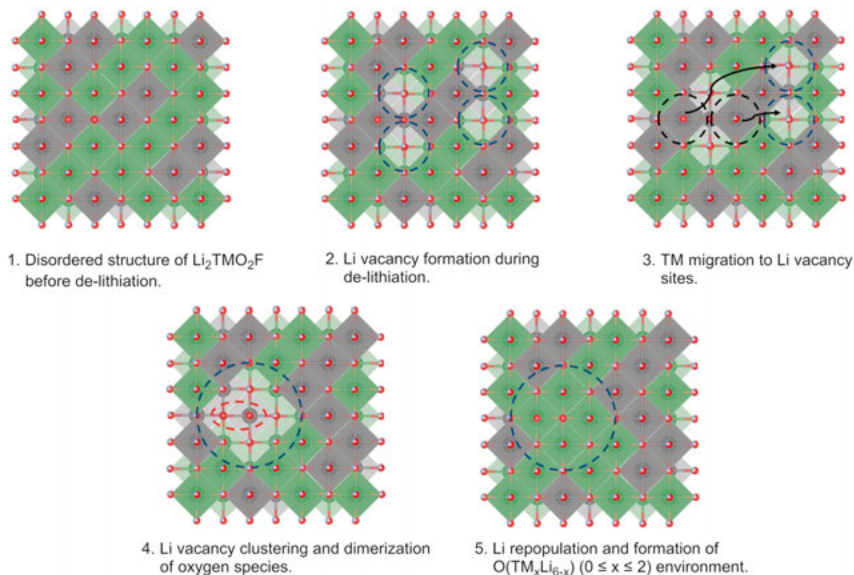


Figure 31. Mechanism for Li vacancy cluster formation, subsequent cation rearrangement and Li repopulation in Li_2TMO_2F . The grey and green octahedrons represent TM and Li environments, respectively.

During repeated insertion and extraction of Li-ions from Li_2VO_2F , it could be expected that the gradual formation, and clustering, of $O(V_xLi_{6-x})$ ($0 \leq x \leq 2$) environments could be manifested in a change not only affecting the local structural motif, but also the average long-range structure of the material. Such a change would then involve a change in the centring type from F-centred to primitive and a consecutive lowering of the symmetry from the space group $Fm\bar{3}m$ to $Pm\bar{3}m$. In the structure described in $Pm\bar{3}m$ symmetry, shown in Figure 32, Li and V preferably, but not exclusively, occupy the $3c$ and $1a$ positions, respectively, with O occupying the $1b$ position and O/F sharing the $3d$ position. In the $Pm\bar{3}m$ space group the 100 reflection is no longer systematically extinct, meaning that the observed peak at $d \approx 4.1$ Å can be indexed. To test this hypothesis, the structure described in the $Pm\bar{3}m$ space group was included in the Rietveld refinement against data collected from the electrochemically cycled Li_2VO_2F . Due to the limited amount of additional observations in the diffraction data, mainly confined to the peak observed at $d \approx 4.1$ Å and changes in relative intensities of the parent DRS structure reflections, constraints on the refined variables were applied. In the model, Li and V occupancies at the $1a$ and $3c$ positions were freely refined, with a maximum V

occupancy at the $3c$ position set to $1/3$ analogous to the $O(V_2Li_4)$ environment. The O and F occupancies at the $3d$ position were fixed according to the parent DRS structure followed by exclusive occupation of O at the $1b$ position, which was then refined freely.

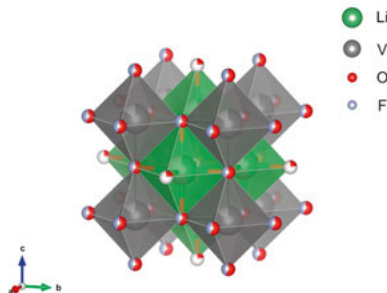


Figure 32. Modelled structure of Li_2VO_2F with clustered Li in $Pm\bar{3}m$ symmetry.

The inclusion of a secondary $Pm\bar{3}m$ phase resulted in an improved overall fit of the observed diffraction data, both for X-rays and neutrons including a fit of the additional reflection at $d \approx 4.1$ Å, as seen in Figure 30. The refined model structure, shown in Figure 32, has a resulting preferential occupation of V and Li at the $1a$ and $3c$ positions, respectively. The refined O occupancy at the $1b$ position was less than unity (0.22), indicating that there was a possible loss of oxygen from the structure. Thus, it would appear as if Li_2VO_2F undergoes cationic re-arrangement, driven by Li vacancy clustering around oxidized O^{n-} -species, as predicted by computational modelling, affecting not only the local structural environments, but also the long-range crystalline structure of the material.

In summary, the findings presented in Paper IV show that the structural behaviour in Li_2VO_2F differs when comparing delithiation over different time domains, i.e. delithiation over an extended (chemical) and shorter period of time (electrochemical). While chemical delithiation tends to favour formation of thermodynamically stable phases (if allowed enough time to reach equilibrium), electrochemical delithiation appears to occur via metastable intermediates, possibly due to the higher rate of delithiation. At low enough currents, the formation of also the thermodynamically stable phases $LiVO_2$ and LiF can be expected. However, it is interesting that the metastable route is preferred already at the relatively slow rate $C/20$. The metastable intermediates were found to possibly involve changes in the local structure due to oxygen dimerization, Li vacancy clustering and cation rearrangement. Upon prolonged electrochemical de- and relithiation, these structural changes are also manifested in the long-range structure through the appearance of a new crystalline phase.

Uncovering the full mechanism of the formation of this new phase nevertheless requires further work, along with a clarification of its role in the electrochemical performance, such as capacity fading, in $\text{Li}_2\text{VO}_2\text{F}$.

5. Conclusions

In this thesis, the equilibrium and non-equilibrium structural behaviour seen for two rock-salt derived battery cathode materials $\text{LiNi}_{0.5}\text{Mn}_{1.5}\text{O}_4$ and $\text{Li}_2\text{VO}_2\text{F}$ has been studied with a focus on crystallography, utilizing both X-ray and neutron diffraction techniques. More specifically, the link between the structural behaviour during electrochemical cycling and the cationic arrangement in their structure were explored.

In the first part, the temperature for Ni and Mn ordering in $\text{LiNi}_{0.5}\text{Mn}_{1.5}\text{O}_4$ was found to be dramatically lowered when Li was removed from the structure, compared to for a fully lithiated material. This could be explained by a lowered energy barrier for the formation of intermediate Frenkel defects, through which the ordering process occurred. Furthermore, NiMn_2O_4 - and NiMnO_3 -type phases formed during heating, where the formation of both phases could be linked to transition metal rearrangement in the structure, following a similar mechanism as Ni and Mn ordering. Therefore, the processes for ordering and formation of these two phases were found to compete with each other, where more ordering led to less formation of the NiMn_2O_4 - and NiMnO_3 -type phases, and vice versa. The growth of NiMnO_3 is linked to oxygen release, driven by reduction of Ni^{4+} , resulting in more NiMnO_3 formation at lower lithium content, whereas ordering was favoured at higher lithium content.

In the second part, a setup for conducting *operando* synchrotron X-ray diffraction measurements was presented. The design combines a standard battery pouch cell with a robust holder where an adjustable and uniform stack pressure can reliably be applied. The setup was shown to be especially suitable for targeting measurements at high rates due to the combination of low ohmic polarisation and simultaneous ability to collect high quality diffraction data. The developed *operando* setup was utilized to study the differences in structural transitions between the disordered and ordered forms of $\text{LiNi}_{0.5}\text{Mn}_{1.5}\text{O}_4$. The mechanism for the first-order transitions in the material involves the formation of a coherent interphase between co-existing phases. With increasing transition metal disorder, the lower the barrier became to form an extended coherent interphase, narrowing the miscibility gap between involved phases. This decrease in miscibility gap could also be seen with increasing applied current density and could be attributed to the movement speed of the coherent interphase becoming rate-limiting, resulting in the formation of a kinetically faster

solid solution. Thus, a solid solution-type behaviour could be induced in $\text{LiNi}_{0.5}\text{Mn}_{1.5}\text{O}_4$ at high current densities.

In the third and final part of this thesis, structural changes in $\text{Li}_2\text{VO}_2\text{F}$ due to prolonged galvanostatic cycling were studied utilizing X-ray and neutron diffraction. The formation of a new crystalline phase, not belonging to either of the thermodynamically stable end phases LiVO_2 and LiF , was observed. From previous insights into the structural behaviour of both layered and DRS Li-rich materials and their similarities to $\text{Li}_2\text{VO}_2\text{F}$, a mechanism involving oxygen dimerization, Li vacancy clustering and cation rearrangement was proposed as an explanation for the appearance of this new phase. Upon re-lithiation, the resulting Li clustering leads to the formation of a structure described in the space group $Pm\bar{3}m$. Interestingly, these findings show that $\text{Li}_2\text{VO}_2\text{F}$ operates in a metastable state also during prolonged galvanostatic cycling. However, the full details of the proposed mechanism need to be further investigated along with its influence on the electrochemical properties of $\text{Li}_2\text{VO}_2\text{F}$. Further investigations, looking into the local structural environment of the formed crystalline phase via e.g. total scattering or nuclear magnetic resonance could also be of interest.

In summary, from the findings on both $\text{LiNi}_{0.5}\text{Mn}_{1.5}\text{O}_4$ and $\text{Li}_2\text{VO}_2\text{F}$, cationic rearrangement appears to play a key role in formation of new phases in the rock-salt derived class of materials. When designing rock-salt derived structures, special consideration should be taken concerning this interplay between cation movement and structural transitions both in production and electrochemical cycling. By understanding the thermodynamical driving forces of phase transitions, predictions on phases formed during electrochemical cycling can be made, as was shown by the work in Paper I. This highlights the need for controlling cationic diffusion in LNMO so as to mitigate the formation of secondary phases and structural reorganization to an electrochemically less ideal configuration. However, for some structure types, the rearrangement of cations during cycling might not lead to formation of the thermodynamically most stable phases, but rather formation of metastable phases, as was shown in Paper IV. The identification of a new phase forming in $\text{Li}_2\text{VO}_2\text{F}$ during cycling can serve as a starting point for further investigations into this new structure and what its possible relation to the rapid capacity fade may be. Further, how the cations arrange can have a direct impact on the phase transition kinetics and dynamics, which was highlighted in Paper II and III. By even a minor introduction of disorder, the barrier for formation of a coherent interphase and solid solution-type behaviour was significantly lowered. This insight can aid in the understanding on the role of cation arrangement for the formation of solid solutions in the disordered rock-salt class of material.

Sammanfattning på Svenska

Implementering och tillämpning av batterier utgör en viktig del i omställningen från fossila bränslen till mer gröna, förnyelsebara energialternativ. Li-jonbatterier spelar, och har spelat, en stor roll i utvecklingen av uppladdningsbara batterier för tillämpning inom bärbar elektronik, och på senare år även elfordon. Ända sedan upptäckten och kommersialiseringen av Li-jonbatteriet har ett stort forskningsfokus legat på att förbättra och optimera tekniken, något som pågår i högsta grad än idag. En utökad tillämpning av tekniken kräver en ständig förbättring och förfining för att möta de olika krav som ställs inom olika tillämpningsområden.

Ett Li-jonbatteri består i huvudsak av fyra olika komponenter; två elektroder (katod och anod), elektrolyt och separator. Katoden och anoden utgör de delar där energin i ett batteri lagras genom att Li-joner förs in och extraheras i dessa material. Framförallt utgör katoden en viktig del av batteriet då denna oftast är den begränsande faktorn till hur mycket energi som kan lagras samt batteriets totala kostnad. Av den anledningen riktas en stor del av forskningen inom Li-jonbatterier mot just katodmaterial, med syftet att hitta nya typer av material som ger en högre kapacitet och bidrar till en lägre kostnad.

För att förstå hur olika katodmaterial fungerar så är det viktigt att undersöka deras kristallstruktur, då det är i strukturen som Li-jonerna reversibelt lagras och extraheras. En användningsbar teknik för att göra detta är genom diffraktion med antingen röntgenstrålning eller neutroner. Med hjälp av diffraktion fås information om den kristallina strukturen hos dessa material på atomnivå, vilket är av stor nytta för att förstå hur Li-joner rör sig in och ut ur strukturen. Även hur strukturen hos materialen ändras under användning är värdefull information som kan erhållas från diffraktion. Detta är speciellt viktigt för material som genomgår stora strukturella förändringar då de cyklas i ett batteri. Generellt anses alltför stor förändring av den kristallina strukturen vara dåligt ur ett långsiktigt perspektiv då det kan leda till batteriet på sikt förlorar en stor del av sin reversibla kapacitet.

Arbetet i denna avhandling fokuserar på att undersöka den kristallina strukturen i två olika katodmaterial och framförallt hur konfigurationen av katjoner i strukturen påverkar dess egenskaper relaterade till användning i ett batteri. I avhandlingens första del undersöktes katodmaterialet $\text{LiNi}_{0.5}\text{Mn}_{1.5}\text{O}_4$ och dess tendens att ändra strukturell konfiguration då Li extraheras ur strukturen. Ge-

nom att studera strukturen under uppvärmning upptäcktes att framförallt övergångsmetallerna (Ni och Mn) migrerar i strukturen, vilket leder till en ny strukturell konfiguration och bildandet av nya sekundära faser. Både bildandet av nya faser, samt den förändrade konfiguration hos $\text{LiNi}_{0.5}\text{Mn}_{1.5}\text{O}_4$ kan anses vara dåliga för materialets prestanda som katodmaterial. Resultaten belyser därmed att framtida optimering av detta material borde inrikta sig på att utveckla strategier för att förhindra migration av övergångsmetaller i strukturen.

I avhandlingens andra del presenteras en experimentell anordning för att undersöka strukturen hos batterimaterial under användning med hjälp av röntgendiffraktion. Då en del av de processer som sker i ett batteri under användning inte sker vid jämvikt, så kan de enbart observeras då batteriet upp- och urladdas. Att förstå dessa processer, som exempelvis fasomvandlingar och ändringar i den kristallina strukturen hos elektrodmaterialen, är en viktig del av förståelsen för hur batterier fungerar. Att genomföra mätningar, som exempelvis diffraktionsexperiment, är dock inte helt enkelt då alla batteriets komponenter kan bidra till de observationer som görs. Ofta innebär detta att batteriets design måste modifieras för att elektrodmaterialen ska kunna studeras. Detta medför i sin tur att batteriets funktion kan rubbas och att det inte presterar optimalt. Den anordning som presenteras här har som syfte att bibehålla batteriets funktion och prestanda, samtidigt som den diffraktionsdata som samlas in gör det möjligt att följa ändringar i strukturen hos elektrodmaterialen. Anordningen demonstrerades genom mätningar på $\text{LiNi}_{0.5}\text{Mn}_{1.5}\text{O}_4$ under upp- och urladdning vid olika strömstyrkor. De kända fasomvandlingarna i materialet kunde observeras, samtidigt som den elektrokemiska prestandan var jämförbar med en vanlig battericell. Den presenterade anordningen kommer att vara ett värdefullt hjälpmedel för fortsatta studier kring strukturella förändringar i elektrodmaterial under användning.

Fortsatt presenteras en mer detaljerad analys av fasomvandlingarna i $\text{LiNi}_{0.5}\text{Mn}_{1.5}\text{O}_4$ och de mekanismer som ligger bakom dessa. Mer specifikt undersöktes hur konfigurationen av övergångsmetallerna i strukturen påverkar dessa mekanismer. Även inverkan av den applicerade strömstyrkan på fasomvandlingarna undersöktes. Resultaten kunde avslöja en trolig mekanism för hur fasomvandlingarna i materialet sker i de kristallina domänerna i materialet. Vidare framkom att en mer oordnad konfiguration av övergångsmetallerna ledde till en mer gynnsam övergång mellan olika faser i materialet, vilket skulle kunna förklara varför denna konfiguration har visat sig vara mer fördelaktig då materialet används i ett batteri.

I avhandlingens sista del studeras materialet $\text{Li}_2\text{VO}_2\text{F}$, tillhörande en ny typ av katodmaterial som undersöks för tillämpning i Li-jonbatterier. Efter ca 100 upp- och urladdningscykler undersöktes den kristallina strukturen med hjälp av diffraktion, vilket resulterade i upptäckten av en ny fas med en annan typ av struktur. Denna struktur kunde kopplas till en omorganisering av katjoner i strukturen. Insikten om att detta material genomgår en fasomvandling kommer att vara till hjälp för att förstå materialets prestanda vid användning i ett

Li-jonbatteri. Framförallt kan insikterna från detta resultat användas i framtida studier kring vilken roll den nya strukturen har i den gradvis minskande kapacitet som ofta observeras för detta material.

Sammantaget visar resultaten i denna avhandling att migration av katjoner spelar en avgörande roll för det strukturella beteendet i båda typerna av material. Då många katodmaterial delar stora likheter strukturellt med de material som undersökts här kan liknande mekanismer, som innefattar omorganisation av katjoner, förväntas ske även i dessa. Därmed uppmuntras en tillämpning av strategier som förhindrar sådan typ av strukturell omorganisering för att optimera prestandan i denna klass av katodmaterial.

Acknowledgements

First, I would like to extend my warmest thank you to my main supervisor Will. Thank you for introducing me to the glorious world of diffraction and for letting me see so many cool synchrotrons and neutron facilities all over the world. It has been a really eventful journey filled with learning. From the first refinements in GSAS on neutron data from JEEP-II (RIP), to hellish multi-bank refinements of *in situ* neutron data in TOPAS. Thank you for always being around for meaningful discussions despite my awful sense of time management and planning. Thank you also to my co-supervisors Mario and Fredrik for providing valuable feedback on my work. Mario, thank you for always dropping by randomly to check how things are going. I have truly appreciated it. To all co-authors, thank you for help with my research work and aiding in writing. Special thanks to Christian for all the hard work with the Li-rich stuff. A special thanks also to Alexander at DESY for invaluable help with beam time. I am extra thankful for the help with the remote beam time.

To all the colleagues in Structural Chemistry and Inorganic Chemistry, I would like to extend a big thanks for making the working environment at Ångström such a nice one. Many thanks to Alina and Fredrik for keeping the lab in good shape. A special thanks to Dickson, Burak and Adriano for extra help around the lab. A big thank you to Leif in the workshop for construction of my experimental setups. Ashok, thank you for company and help during beam times and also for all sports- and TOPAS-related discussions. The beam time at ANSTO was truly a great journey and it was kind of you to let me come along. Gustav, you also deserve a big thanks for any diffraction related discussions, may your multi-bank neutron TOF refinements forever converge fast! Thanks also for the company and hard work when repairing the good ol' STOE. At least we got to truly see what the inside of a diffractometer looks like. A kind thanks to Håkan and Torbjörn for help in the reparation is also appropriate. To Sarmad, I thank you for stellar company in the office and being the best of office-mates. It was nice to share some laughs when things were at their most stressful. Also, a big thanks to Ida, Agnes and Alexandra for beam time company. For people outside the department, I would like to extend a thank you to Albert and Simon at Nanotechnology and Functional Materials. Thank you for accepting me as a master thesis worker and for letting me in on your work on nanocellulose and also, to quote Simon, "filtrating toilet water". Without you, I would have never ended up here.

Finally, I would like to thank the people that have meant the most to me, not only as support during my PhD studies, but for the most important part – life outside of science. Emil, Gustav, Krille, Zacke, Daniel, Babak, Jonas och Leo. Finare vänner går inte att hitta och jag är så otroligt glad över att jag har er. Emil, Håkan och Eric, vi blev kanske aldrig några rock-stjärnor, men jäklar vad kul vi har haft det i repen. Tack för det! Till min bästa vän Eric, jag är så otroligt glad att jag har dig och att du har stått ut med mig alla dessa år. Jag ser fram emot att fortsätta våra äventyr tillsammans, även när vi blivit gamla gubbar. Till min familj hemma i Dala-Floda, jag kommer aldrig sluta längta tills nästa gång jag får åka hem och träffa er. Tack Mormor och Hasse för allt fika och allt skjutsande till träningar och matcher. Det har betytt väldigt mycket. Tack Mamma, Pappa, Linnea och Joel, det här hade aldrig gått utan er. Det går inte att önska sig en bättre familj och stöd. Mamma och pappa, den här avhandlingen är till er. Viktor och Gunnar, jag är så himla glad att ni tillkommit under resans gång. Till sist, min älskade Johanna, tack för att du alltid stöttat mig under den här resan och trott på mig, framförallt när jag själv gjort det som minst. Du har varit den som gjort att jag tagit mig igenom detta många gånger och jag kommer för alltid att vara tacksam för det. Nu ser jag fram emot att fortsätta upptäcka världen med dig.

References

1. Masson-Delmotte, V., P. Zhai, A. Pirani, S.; L. Connors, C. P., S. Berger, N. Caud, Y. Chen, L. Goldfarb, M. I. Gomis, M. Huang, K. Leitzell, E. Lonnoy, J. B.; R. Matthews, T. K. M., T. Waterfield, O. Yelekçi, R. Yu and B. Zhou (eds.) *Climate Change 2021: The Physical Science Basis. Contribution of Working Group I to the Sixth Assessment Report of the Intergovernmental Panel on Climate Change*; IPCC: 2021.
2. *Make Transport Greener*; European Commission: 2021.
3. Whittingham, M. S., Electrical Energy Storage and Intercalation Chemistry. *Science* **1976**, 192 (4244), 1126-1127.
4. Mizushima, K.; Jones, P. C.; Wiseman, P. J.; Goodenough, J. B., Li_xCoO_2 ($0 < x < 1$): A new cathode material for batteries of high energy density. *Mater. Res. Bull.* **1980**, 15 (6), 783-789.
5. Yoshino, A.; Sanechika, K.; Nakajima, T. Secondary Battery. US patent no. 4,668,595, 1987.
6. Wentker, M.; Greenwood, M.; Leker, J., A Bottom-Up Approach to Lithium-Ion Battery Cost Modeling with a Focus on Cathode Active Materials. *Energies* **2019**, 12 (3), 504.
7. Pecharsky, V. K.; Zavalij, P. Y., *Fundamentals of powder diffraction and structural characterization of materials*. 2nd ed.; Springer: New York, 2009.
8. Eftekhari, A., Lithium-Ion Batteries with High Rate Capabilities. *ACS Sustainable Chemistry & Engineering* **2017**, 5 (4), 2799-2816.
9. Kang, K.; Ceder, G., Factors that affect Li mobility in layered lithium transition metal oxides. *Phys. Rev. B* **2006**, 74 (9), 094105.
10. Lee, W.; Muhammad, S.; Sergey, C.; Lee, H.; Yoon, J.; Kang, Y.-M.; Yoon, W.-S., Advances in the Cathode Materials for Lithium Rechargeable Batteries. *Angew. Chem. Int. Ed.* **2020**, 59 (7), 2578-2605.
11. Euchner, H.; Chang, J. H.; Groß, A., On stability and kinetics of Li-rich transition metal oxides and oxyfluorides. *J. Mater. Chem. A* **2020**, 8 (16), 7956-7967.
12. Kang, K.; Meng, Y. S.; Bréger, J.; Grey, C. P.; Ceder, G., Electrodes with High Power and High Capacity for Rechargeable Lithium Batteries. *Science* **2006**, 311 (5763), 977-980.
13. Xia, H.; Meng, Y. S.; Lu, L.; Ceder, G., Electrochemical Properties of Non-stoichiometric $\text{LiNi}_{0.5}\text{Mn}_{1.5}\text{O}_{4-\delta}$ Thin-Film Electrodes Prepared by Pulsed Laser Deposition. *J. Electrochem. Soc.* **2007**, 154 (8), A737-A743.
14. Aktekin, B.; Massel, F.; Ahmadi, M.; Valvo, M.; Hahlin, M.; Zipprich, W.; Marzano, F.; Duda, L.; Younesi, R.; Edström, K.; Brandell, D., How Mn/Ni Ordering Controls Electrochemical Performance in High-Voltage Spinel $\text{LiNi}_{0.44}\text{Mn}_{1.56}\text{O}_4$ with Fixed Oxygen Content. *ACS Appl. Energy Mater.* **2020**, 3 (6), 6001-6013.

15. Ryoo, H.; Bae, H. B.; Kim, Y.-M.; Kim, J.-G.; Lee, S.; Chung, S.-Y., Frenkel-Defect-Mediated Chemical Ordering Transition in a Li–Mn–Ni Spinel Oxide. *Angew. Chem. Int. Ed.* **2015**, *54* (27), 7963-7967.
16. Kreller, C. R.; Uberuaga, B. P., The role of cation ordering and disordering on mass transport in complex oxides. *Curr. Opin. Solid State Mater. Sci.* **2021**, *25* (2), 100899.
17. Manthiram, A.; Chemelewski, K.; Lee, E.-S., A perspective on the high-voltage LiMn_{1.5}Ni_{0.5}O₄ spinel cathode for lithium-ion batteries. *Energy Environ. Sci.* **2014**, *7* (4), 1339-1350.
18. Song, B.; Veith, G. M.; Park, J.; Yoon, M.; Whitfield, P. S.; Kirkham, M. J.; Liu, J.; Huq, A., Metastable Li_{1+δ}Mn₂O₄ (0 ≤ δ ≤ 1) Spinel Phases Revealed by in Operando Neutron Diffraction and First-Principles Calculations. *Chem. Mater.* **2019**, *31* (1), 124-134.
19. Liu, H.; Strobridge, F. C.; Borkiewicz, O. J.; Wiaderek, K. M.; Chapman, K. W.; Chupas, P. J.; Grey, C. P., Capturing metastable structures during high-rate cycling of LiFePO₄ nanoparticle electrodes. *Science* **2014**, *344* (6191), 1252817.
20. Saurel, D.; Galceran, M.; Reynaud, M.; Anne, H.; Casas-Cabanas, M., Rate dependence of the reaction mechanism in olivine NaFePO₄ Na-ion cathode material. *Int. J. Energy Res.* **2018**, *42* (10), 3258-3265.
21. Zhou, Y.-N.; Yue, J.-L.; Hu, E.; Li, H.; Gu, L.; Nam, K.-W.; Bak, S.-M.; Yu, X.; Liu, J.; Bai, J.; Dooryhee, E.; Fu, Z.-W.; Yang, X.-Q., High-Rate Charging Induced Intermediate Phases and Structural Changes of Layer-Structured Cathode for Lithium-Ion Batteries. *Adv. Energy Mater.* **2016**, *6* (21), 1600597.
22. Baur, C.; Lăcătușu, M.-E.; Fichtner, M.; Johnsen, R. E., Insights into Structural Transformations in the Local Structure of Li₂VO₂F Using Operando X-ray Diffraction and Total Scattering: Amorphization and Recrystallization. *ACS Appl. Mater. Interfaces* **2020**, *12* (24), 27010-27016.
23. Strobridge, F. C.; Orvananos, B.; Croft, M.; Yu, H.-C.; Robert, R.; Liu, H.; Zhong, Z.; Connolly, T.; Drakopoulos, M.; Thornton, K.; Grey, C. P., Mapping the Inhomogeneous Electrochemical Reaction Through Porous LiFePO₄-Electrodes in a Standard Coin Cell Battery. *Chem. Mater.* **2015**, *27* (7), 2374-2386.
24. Padhi, A. K.; Nanjundaswamy, K. S.; Goodenough, J. B., Phospho-olivines as Positive-Electrode Materials for Rechargeable Lithium Batteries. *J. Electrochem. Soc.* **1997**, *144* (4), 1188-1194.
25. Sharma, N.; Guo, X.; Du, G.; Guo, Z.; Wang, J.; Wang, Z.; Peterson, V. K., Direct Evidence of Concurrent Solid-Solution and Two-Phase Reactions and the Nonequilibrium Structural Evolution of LiFePO₄. *J. Am. Chem. Soc.* **2012**, *134* (18), 7867-7873.
26. Malik, R.; Abdellahi, A.; Ceder, G., A Critical Review of the Li Insertion Mechanisms in LiFePO₄ Electrodes. *J. Electrochem. Soc.* **2013**, *160* (5), A3179-A3197.
27. Liang, G.; Hao, J.; D'Angelo, A. M.; Peterson, V. K.; Guo, Z.; Pang, W. K., A Robust Coin-Cell Design for In Situ Synchrotron-based X-Ray Powder Diffraction Analysis of Battery Materials. *Batteries Supercaps* **2021**, *4* (2), 380-384.
28. Borkiewicz, O. J.; Wiaderek, K. M.; Chupas, P. J.; Chapman, K. W., Best Practices for Operando Battery Experiments: Influences of X-ray Experiment Design on Observed Electrochemical Reactivity. *J. Phys. Chem. Lett.* **2015**, *6* (11), 2081-2085.

29. Liu, D.; Shadike, Z.; Lin, R.; Qian, K.; Li, H.; Li, K.; Wang, S.; Yu, Q.; Liu, M.; Ganapathy, S.; Qin, X.; Yang, Q.-H.; Wagemaker, M.; Kang, F.; Yang, X.-Q.; Li, B., Review of Recent Development of In Situ/Operando Characterization Techniques for Lithium Battery Research. *Adv. Mater.* **2019**, *31* (28), 1806620.
30. Delacourt, C.; Poizot, P.; Tarascon, J.-M.; Masquelier, C., The existence of a temperature-driven solid solution in Li_xFePO_4 for $0 \leq x \leq 1$. *Nat. Mater.* **2005**, *4*, 254-260.
31. Chen, R.; Ren, S.; Knapp, M.; Wang, D.; Witter, R.; Fichtner, M.; Hahn, H., Disordered Lithium-Rich Oxyfluoride as a Stable Host for Enhanced Li^+ Intercalation Storage. *Adv. Energy Mater.* **2015**, *5* (9), 1401814.
32. Wang, X. Y.; Huang, Y. Q.; Ji, D. S.; Omenya, F.; Karki, K.; Sallis, S.; Piper, L. F. J.; Wiaderek, K. M.; Chapman, K. W.; Chernova, N. A.; Whittingham, M. S., Structure Evolution and Thermal Stability of High-Energy-Density Li-Ion Battery Cathode $\text{Li}_2\text{VO}_2\text{F}$. *J. Electrochem. Soc.* **2017**, *164* (7), A1552-A1558.
33. Baur, C.; Källquist, I.; Chable, J.; Chang, J. H.; Johnsen, R. E.; Ruiz-Zepeda, F.; Ateba Mba, J.-M.; Naylor, A. J.; Garcia-Lastra, J. M.; Vegge, T.; Klein, F.; Schür, A. R.; Norby, P.; Edström, K.; Hahlin, M.; Fichtner, M., Improved cycling stability in high-capacity Li-rich vanadium containing disordered rock salt oxyfluoride cathodes. *J. Mater. Chem. A* **2019**, *7* (37), 21244-21253.
34. Chang, J. H.; Baur, C.; Ateba Mba, J.-M.; Arçon, D.; Mali, G.; Alwast, D.; Behm, R. J.; Fichtner, M.; Vegge, T.; Garcia Lastra, J. M., Superoxide formation in $\text{Li}_2\text{VO}_2\text{F}$ cathode material – a combined computational and experimental investigation of anionic redox activity. *J. Mater. Chem. A* **2020**, *8* (32), 16551-16559.
35. Chable, J.; Baur, C.; Chang, J. H.; Wenzel, S.; García-Lastra, J. M.; Vegge, T., From Trigonal to Cubic LiVO_2 : A High-Energy Phase Transition toward Disordered Rock Salt Materials. *J. Phys. Chem. C* **2020**, *124* (3), 2229-2237.
36. Uyama, T.; Mukai, K.; Yamada, I., High-Pressure Synthesis of Cation-Disordered Rock-Salt Oxyfluorides with High Crystallinity. *Electrochemistry (Tokyo, Jpn.)* **2021**, *89* (2), 94-99.
37. Baur, C.; Chable, J.; Klein, F.; Chakravadhanula, V. S. K.; Fichtner, M., Reversible Delithiation of Disordered Rock Salt LiVO_2 . *ChemElectroChem* **2018**, *5* (11), 1484-1490.
38. Bragg, W. H.; Bragg, W. L., The reflection of X-rays by crystals. *Proceedings of the Royal Society of London. Series A, Containing Papers of a Mathematical and Physical Character* **1913**, *88* (605), 428-438.
39. Dippel, A.-C.; Liermann, H.-P.; Delitz, J. T.; Walter, P.; Schulte-Schrepping, H.; Seeck, O. H.; Franz, H., Beamline P02.1 at PETRA III for high-resolution and high-energy powder diffraction. *J. Synchrotron Radiat.* **2015**, *22* (3), 675-687.
40. Smith, R. I.; Hull, S.; Tucker, M. G.; Playford, H. Y.; McPhail, D. J.; Waller, S. P.; Norberg, S. T., The upgraded Polaris powder diffractometer at the ISIS neutron source. *Rev. Sci. Instrum.* **2019**, *90* (11), 115101.
41. Williams, W. G.; Ibberson, R. M.; Day, P.; Enderby, J. E., GEM — General materials diffractometer at ISIS. *Physica B: Condensed Matter* **1997**, *241*-243, 234-236.
42. Avdeev, M.; Hester, J. R., ECHIDNA: a decade of high-resolution neutron powder diffraction at OPAL. *J. Appl. Crystallogr.* **2018**, *51* (6), 1597-1604.
43. Rietveld, H. M., Line profiles of neutron powder-diffraction peaks for structure refinement. *Acta Crystallogr.* **1967**, *22* (1), 151-152.

44. Rietveld, H. M., A profile refinement method for nuclear and magnetic structures. *J. Appl. Crystallogr.* **1969**, 2 (2), 65-71.
45. Dinnebier, R. E.; Leineweber, A.; Evans, J. S. O., *Rietveld refinement: practical powder diffraction pattern analysis using TOPAS*. De Gruyter: Berlin/Boston, 2019.
46. Coelho, A., TOPAS and TOPAS-Academic: an optimization program integrating computer algebra and crystallographic objects written in C++. *J. Appl. Crystallogr.* **2018**, 51 (1), 210-218.
47. Cheary, R. W.; Coelho, A. A.; Cline, J. P., Fundamental parameters line profile fitting in laboratory diffractometers. *J. Res. Natl. Inst. Stand. Technol.* **2004**, 109 (1), 1-25.
48. Strobridge, F. C.; Liu, H.; Leskes, M.; Borkiewicz, O. J.; Wiaderek, K. M.; Chupas, P. J.; Chapman, K. W.; Grey, C. P., Unraveling the Complex Delithiation Mechanisms of Olivine-Type Cathode Materials, LiFe_{0.5}Co_{1-x}PO₄. *Chem. Mater.* **2016**, 28 (11), 3676-3690.
49. Warren, B. E., *X-ray diffraction*. Dover: New York, 1990.
50. Morrison, C.; Sun, H.; Yao, Y.; Loomis, R. A.; Buhro, W. E., Methods for the ICP-OES Analysis of Semiconductor Materials. *Chem. Mater.* **2020**, 32 (5), 1760-1768.
51. Aktekin, B.; Valvo, M.; Smith, R. I.; Sørby, M. H.; Lodi Marzano, F.; Zipprich, W.; Brandell, D.; Edström, K.; Brant, W. R., Cation Ordering and Oxygen Release in LiNi_{0.5-x}Mn_{1.5+x}O_{4-y} (LNMO): In Situ Neutron Diffraction and Performance in Li Ion Full Cells. *ACS Appl. Energy Mater.* **2019**, 2 (5), 3323-3335.
52. Cai, L.; Liu, Z.; An, K.; Liang, C., Unraveling structural evolution of LiNi_{0.5}Mn_{1.5}O₄ by in situ neutron diffraction. *J. Mater. Chem. A* **2013**, 1 (23), 6908-6914.
53. Kim, J.-H.; Huq, A.; Chi, M.; Pieczonka, N. P. W.; Lee, E.; Bridges, C. A.; Tessema, M. M.; Manthiram, A.; Persson, K. A.; Powell, B. R., Integrated Nano-Domains of Disordered and Ordered Spinel Phases in LiNi_{0.5}Mn_{1.5}O₄ for Li-Ion Batteries. *Chem. Mater.* **2014**, 26 (15), 4377-4386.
54. Hu, E.; Bak, S.-M.; Liu, J.; Yu, X.; Zhou, Y.; Ehrlich, S. N.; Yang, X.-Q.; Nam, K.-W., Oxygen-Release-Related Thermal Stability and Decomposition Pathways of Li_xNi_{0.5}Mn_{1.5}O₄ Cathode Materials. *Chem. Mater.* **2014**, 26 (2), 1108-1118.
55. Bianchini, M.; Fauth, F.; Suard, E.; Leriche, J.-B.; Masquelier, C.; Croguennec, L., Spinel materials for Li-ion batteries: new insights obtained by operando neutron and synchrotron X-ray diffraction. *AcCrB* **2015**, 71 (6), 688-701.
56. Kishida, I.; Orita, K.; Nakamura, A.; Yokogawa, Y., Thermodynamic analysis using first-principles calculations of phases and structures of Li_xNi_{0.5}Mn_{1.5}O₄ (0 ≤ x ≤ 1). *J. Power Sources* **2013**, 241, 1-5.
57. Nam, K.-W.; Bak, S.-M.; Hu, E.; Yu, X.; Zhou, Y.; Wang, X.; Wu, L.; Zhu, Y.; Chung, K.-Y.; Yang, X.-Q., Combining In Situ Synchrotron X-Ray Diffraction and Absorption Techniques with Transmission Electron Microscopy to Study the Origin of Thermal Instability in Overcharged Cathode Materials for Lithium-Ion Batteries. *Adv. Funct. Mater.* **2013**, 23 (8), 1047-1063.
58. Cloud, W. H., Crystal Structure and Ferrimagnetism in NiMnO₃ and CoMnO₃. *Physical Review* **1958**, 111 (4), 1046-1049.
59. Sagua, A.; Lescano, G. M.; Alonso, J. A.; Martínez-Coronado, R.; Fernández-Díaz, M. T.; Morán, E., Neutron structural characterization, inversion degree and transport properties of NiMn₂O₄ spinel prepared by the hydroxide route. *Mater. Res. Bull.* **2012**, 47 (6), 1335-1338.

60. Lin, Z.; Liu, T.; Ai, X.; Liang, C., Aligning academia and industry for unified battery performance metrics. *Nat. Commun.* **2018**, *9* (1), 5262.
61. Komatsu, H.; Arai, H.; Koyama, Y.; Sato, K.; Kato, T.; Yoshida, R.; Murayama, H.; Takahashi, I.; Orikasa, Y.; Fukuda, K.; Hirayama, T.; Ikuhara, Y.; Ukyo, Y.; Uchimoto, Y.; Ogumi, Z., Solid Solution Domains at Phase Transition Front of $\text{Li}_{0.5}\text{Ni}_{0.5}\text{Mn}_{1.5}\text{O}_4$. *Adv. Energy Mater.* **2015**, *5* (17), 1500638.
62. Ma, X.; Kang, B.; Ceder, G., High Rate Micron-Sized Ordered $\text{LiNi}_{0.5}\text{Mn}_{1.5}\text{O}_4$. *J. Electrochem. Soc.* **2010**, *157* (8), A925-A931.
63. Ravnsbæk, D. B.; Xiang, K.; Xing, W.; Borkiewicz, O. J.; Wiaderek, K. M.; Gionet, P.; Chapman, K. W.; Chupas, P. J.; Chiang, Y. M., Extended Solid Solutions and Coherent Transformations in Nanoscale Olivine Cathodes. *Nano Lett.* **2014**, *14* (3), 1484-1491.
64. Zhang, X.; van Hulzen, M.; Singh, D. P.; Brownrigg, A.; Wright, J. P.; van Dijk, N. H.; Wagemaker, M., Rate-Induced Solubility and Suppression of the First-Order Phase Transition in Olivine LiFePO_4 . *Nano Lett.* **2014**, *14* (5), 2279-2285.
65. Goodenough, J. B.; Kim, Y., Challenges for Rechargeable Li Batteries. *Chem. Mater.* **2010**, *22* (3), 587-603.
66. Takahashi, I.; Arai, H.; Murayama, H.; Sato, K.; Komatsu, H.; Tanida, H.; Koyama, Y.; Uchimoto, Y.; Ogumi, Z., Phase transition kinetics of $\text{LiNi}_{0.5}\text{Mn}_{1.5}\text{O}_4$ analyzed by temperature-controlled operando X-ray absorption spectroscopy. *Phys. Chem. Chem. Phys.* **2016**, *18* (3), 1897-1904.
67. Lee, E.; Persson, K. A., Solid-Solution Li Intercalation as a Function of Cation Order/Disorder in the High-Voltage $\text{Li}_{0.5}\text{Ni}_{0.5}\text{Mn}_{1.5}\text{O}_4$ Spinel. *Chem. Mater.* **2013**, *25* (14), 2885-2889.
68. Arai, H.; Sato, K.; Orikasa, Y.; Murayama, H.; Takahashi, I.; Koyama, Y.; Uchimoto, Y.; Ogumi, Z., Phase transition kinetics of $\text{LiNi}_{0.5}\text{Mn}_{1.5}\text{O}_4$ electrodes studied by in situ X-ray absorption near-edge structure and X-ray diffraction analysis. *J. Mater. Chem. A* **2013**, *1* (35), 10442-10449.
69. Takahashi, I.; Murayama, H.; Sato, K.; Naka, T.; Kitada, K.; Fukuda, K.; Koyama, Y.; Arai, H.; Matsubara, E.; Uchimoto, Y.; Ogumi, Z., Kinetically asymmetric charge and discharge behavior of $\text{LiNi}_{0.5}\text{Mn}_{1.5}\text{O}_4$ at low temperature observed by in situ X-ray diffraction. *J. Mater. Chem. A* **2014**, *2* (37), 15414-15419.
70. Mather, G. C.; Dussarrat, C.; Etourneau, J.; West, A. R., A review of cation-ordered rock salt superstructure oxides. *J. Mater. Chem.* **2000**, *10* (10), 2219-2230.
71. Gent, W. E.; Lim, K.; Liang, Y.; Li, Q.; Barnes, T.; Ahn, S.-J.; Stone, K. H.; McIntire, M.; Hong, J.; Song, J. H.; Li, Y.; Mehta, A.; Ermon, S.; Tylliszczak, T.; Kilcoyne, D.; Vine, D.; Park, J.-H.; Doo, S.-K.; Toney, M. F.; Yang, W.; Prendergast, D.; Chueh, W. C., Coupling between oxygen redox and cation migration explains unusual electrochemistry in lithium-rich layered oxides. *Nat. Commun.* **2017**, *8* (1), 2091.
72. House, R. A.; Rees, G. J.; Pérez-Osorio, M. A.; Marie, J.-J.; Boivin, E.; Robertson, A. W.; Nag, A.; Garcia-Fernandez, M.; Zhou, K.-J.; Bruce, P. G., First-cycle voltage hysteresis in Li-rich 3d cathodes associated with molecular O_2 trapped in the bulk. *Nat. Energy* **2020**, *5* (10), 777-785.
73. Chen, H.; Islam, M. S., Lithium Extraction Mechanism in Li-Rich Li_2MnO_3 Involving Oxygen Hole Formation and Dimerization. *Chem. Mater.* **2016**, *28* (18), 6656-6663.

74. Hong, J.; Gent, W. E.; Xiao, P.; Lim, K.; Seo, D.-H.; Wu, J.; Csernica, P. M.; Takacs, C. J.; Nordlund, D.; Sun, C.-J.; Stone, K. H.; Passarello, D.; Yang, W.; Prendergast, D.; Ceder, G.; Toney, M. F.; Chueh, W. C., Metal–oxygen decoordination stabilizes anion redox in Li-rich oxides. *Nat. Mater.* **2019**, *18* (3), 256-265.
75. Sharpe, R.; House, R. A.; Clarke, M. J.; Förstermann, D.; Marie, J.-J.; Cibir, G.; Zhou, K.-J.; Playford, H. Y.; Bruce, P. G.; Islam, M. S., Redox Chemistry and the Role of Trapped Molecular O₂ in Li-Rich Disordered Rocksalt Ox-
yfluoride Cathodes. *J. Am. Chem. Soc.* **2020**, *142* (52), 21799-21809.
76. Ben Yahia, M.; Vergnet, J.; Saubanère, M.; Doublet, M.-L., Unified picture of anionic redox in Li/Na-ion batteries. *Nat. Mater.* **2019**, *18* (5), 496-502.
77. Li, X.; Qiao, Y.; Guo, S.; Xu, Z.; Zhu, H.; Zhang, X.; Yuan, Y.; He, P.; Ishida, M.; Zhou, H., Direct Visualization of the Reversible O₂–/O– Redox Process in Li-Rich Cathode Materials. *Adv. Mater.* **2018**, *30* (14), 1705197.
78. McCalla, E.; Abakumov, A. M.; Saubanère, M.; Foix, D.; Berg, E. J.; Rousse, G.; Doublet, M.-L.; Gonbeau, D.; Novák, P.; Van Tendeloo, G.; Dominko, R.; Tarascon, J.-M., Visualization of O-O peroxo-like dimers in high-capacity layered oxides for Li-ion batteries. *Science* **2015**, *350* (6267), 1516-1521.

Acta Universitatis Upsaliensis

*Digital Comprehensive Summaries of Uppsala Dissertations
from the Faculty of Science and Technology 2194*

Editor: The Dean of the Faculty of Science and Technology

A doctoral dissertation from the Faculty of Science and Technology, Uppsala University, is usually a summary of a number of papers. A few copies of the complete dissertation are kept at major Swedish research libraries, while the summary alone is distributed internationally through the series Digital Comprehensive Summaries of Uppsala Dissertations from the Faculty of Science and Technology. (Prior to January, 2005, the series was published under the title "Comprehensive Summaries of Uppsala Dissertations from the Faculty of Science and Technology".)



ACTA
UNIVERSITATIS
UPSALIENSIS
UPPSALA
2022

Distribution: publications.uu.se
urn:nbn:se:uu:diva-485227